8

Mesoscale and Small-Scale Structure of the Subauroral Geospace

Evgeny Mishin[1] and Anatoly Streltsov[2]

ABSTRACT

A review is given of the current state-of-the-art of experimental studies and the theoretical understanding of mesoscale and small-scale structure of the subauroral geospace, connecting ionospheric structures to plasma wave processes in the turbulent plasmasphere boundary layer (TPBL). Free energy for plasma waves comes from diamagnetic electron and ion currents in the entry layer near the plasma sheet boundary and near the TPBL inner boundary, respectively, and anisotropic distributions of energetic ions inside the TPBL and interior to the inner boundary. Collisionless heating of the plasmaspheric particles gives downward heat and suprathermal electron fluxes sufficient to provide the F-region electron temperature greater than 6000 K. This leads to the formation of specific density troughs in the ionospheric regions in the absence of strong electric fields and upward plasma flows. Small-scale MHD wave structures (SAPSWS) and irregular density troughs emerge on the duskside, coincident with the substorm current wedge development. Numerical simulations show that the ionospheric feedback instability significantly contributes to the SAPSWS formation. Antiparallel temperature and density gradients inside the subauroral troughs lead to the temperature gradient instability. The latter and the gradient-drift instability lead to enhanced decameter-scale irregularities responsible for subauroral HF radar backscatter.

8.1. INTRODUCTION

The midlatitude ionosphere features the mesoscale (typically a few degrees wide in latitude) ionospheric trough (e.g., Rodger, 2008), collocated with a measurable enhancement of the electron temperature and Stable Auroral Red (SAR) arcs (e.g., Prölls, 2006; Foster et al., 1994). It was a common belief in the past that storm-time midlatitude irregularities occur in the expanded auroral zone, until enhanced radar backscatter (Foster & Rich, 1998; Erickson et al., 2002; Mishin et al., 2002) and scintillations of UHF and GPS signals (Basu et al., 2001, 2008; Ledvina et al., 2002) were reported at subauroral latitudes. The subauroral ionosphere maps along the magnetic field (B_0) into the inner magnetosphere, including the ring current (RC) and outer plasmasphere adjacent to the electron plasma sheet (PS) boundary. This magnetosphere-ionosphere region is called the subauroral geospace.

Statistically (e.g., Yizengaw & Moldwin, 2005), the ionospheric trough is adjacent to the ionospheric footprint of the plasmasphere boundary, the plasmapause. The plasmapause is the critical feature of the inner magnetosphere, as indicated by the long-known plasmaspheric "hot zone"

[1]*Air Force Research Laboratory Space Vehicles Directorate, Kirtland Air Force Base, Albuquerque, NM, USA*

[2]*Department of Physical Sciences, Embry-Riddle Aeronautical University, Daytona Beach, FL, USA*

Space Physics and Aeronomy Collection Volume 3: Ionosphere Dynamics and Applications, Geophysical Monograph 260, First Edition.
Edited by Chaosong Huang and Gang Lu.

DOI: 10.1002/9781119815617.ch8

(Gringauz, 1983; Horwitz et al., 1986; Afonin et al., 1997) and the remarkable correlation of the innermost plasmapause location with the radiation belt inner boundary (Goldstein et al., 2005a; Li et al., 2006; Foster et al., 2016). Carpenter and Lemaire (2004) suggested that the plasmapause region be called the plasmasphere boundary layer (PBL) and be considered as a framework for examining interaction between the hot PS and cold plasmasphere plasmas. Such a framework is particularly important for understanding enhanced mesoscale subauroral flows, such as premidnight subauroral ion drifts (SAID) and duskside subauroral polarization streams (SAPS), that rapidly arise in the PBL during disturbed periods and strongly impact the subauroral geospace.

Recent observations suggest (Puhl-Quinn et al., 2007; Mishin & Puhl-Quinn, 2007; Mishin et al., 2010, 2017; Mishin, 2013) that SAID are an integral part of the overarching process of penetration into the plasmasphere of mesoscale (hot) plasma flows (MPFs), earthbound-ejected from the reconnection site. The MPF's electron population is arrested at the plasmapause when the plasmaspheric density exceeds $n_c \sim 10$ cm^{-3} and shorts out the polarization charge at the MPF's front. The hot ions move farther inward until being stopped by the emerging SAID electric field. Mapped into the ionosphere, SAID could be located on the trough's poleward boundary due to the trough-plasmapause statistical relation (e.g., Yizengaw & Moldwin, 2005). The overall process is inherently unstable, so a turbulent PBL (henceforth, TPBL) is created between the PS boundary and the tip of the hot ion flux. The natural result of this process is the close relation of the PS boundary to the plasmapause, the narrow width of SAID, and the abrupt dispersionless PS boundary (cf. Newell & Meng, 1987).

SAID can be formed even during pseudobreakups, while SAPS occur due to the sunward expansion of the substorm current wedge (SCW) (Mishin et al., 2017). SAPS are inherent in the two-loop model of the SCW (e.g., Kepko et al., 2015), with the second current loop (R2L) providing partial closure of the upward (R1L) current at the SCW front through the partial ring current and the R2L downward current at subauroral latitudes. The poleward (SAPS) electric field emerges at the front to drive the meridional (Pedersen) current in the circuit. The resulting E x B drift drives particles sunward with an average speed equal to the front speed, thereby leading to fast RC injections on the duskside. Auroral and subauroral flows in the vicinity of the R1L current connect continuously over the local auroral boundary (e.g., Fig. 9 in Kepko et al., 2015).

Overall, the SCW development is intermittent and unstable. This is consistent with quasi-periodic, small-scale ($\sim$tens km in the ionosphere), SAPS wave structures (SAPSWS) during substorm breakups (Mishin et al., 2003, 2017; Mishin & Burke, 2005; Califf et al., 2016). The peak-to-peak variability, δE, in strong SAPSWS is of the same order as the mean amplitude, E_0, or even greater ($\delta E \geq E_0$); the latter can be sometimes mistaken for multiple SAID. The small-scale structures decay in less than one hour after substorm onsets, leaving smooth (SAPS) envelopes in place (Mishin & Burke, 2005). Several mechanisms have been suggested since the discovery of SAPSWS, yet their generation is not completely understood (see section 8.4, Discussion).

Mishin and Blaunstein (2008) reported on short-scale ionospheric irregularities of ≥800 m wavelengths (the observational limit) observed by the DMSP spacecraft in the SAPSWS region coincident with strong UHF and GPS scintillations. Decameter-scale irregularities at midlatitudes were detected by the DEMETER satellite (Pfaff et al., 2008, Plate 1) and the SuperDARN radars (e.g., Parkinson et al., 2005; Koustov et al., 2006; Oksavik et al.; 2006; Makarevich et al., 2011; Makarevich & Bristow, 2014), and down to a fraction of a meter by incoherent scatter radars (ISRs) (e.g., Erickson et al., 2002; Mishin et al., 2002; Foster et al., 2004). The gradient-drift (GDI) and the temperature-gradient (TGI) instabilities are considered as their major mechanisms (e.g., Keskinen & Huba, 1990; Guzdar et al.,1998; Keskinen et al., 2004; Greenwald et al., 2006; Eltrass & Scales, 2014). The TGI requires that gradients of the plasma density and temperature in the plane perpendicular to B_0 be antiparallel, that is, $\nabla_\perp n \cdot \nabla_\perp T < 0$ (e.g., Kadomtsev, 1965).

Another important effect of elevated ion and electron temperatures is the intensification of charge exchange

$$O^+ + X_2^{(1,2)} \xrightarrow{k_{1,2}} X^{(1,2)}O^+ + X^{(1,2)}, \qquad (8.1)$$

where $X^{(1)}/X^{(2)}$ stands for atomic nitrogen/oxygen (N/O). Indeed, the rate coefficients $k_{1,2}$ increase with the kinetic (thermal and drift) and internal (vibrational) energies of interacting species (e.g., Viggiano & Williams, 2001). The vibrational energy of N_2 and O_2 increases with the electron temperature, T_e, due to electron impact. The presence of vibrationally excited molecules ultimately leads to enhanced recombination of molecular ions and depletion of the F-region plasma in addition to that caused by the E x B-drifting and heated ions and ion outflows (e.g., Newton & Walker, 1975; Schunk et al., 1976; Anderson et al., 1991; Moffett et al., 1998; Pavlov et al., 2000; Mishin et al., 2004).

The ion temperature, T_i, increases due to ohmic heating, while the F-region electrons are mainly heated by heat flux and suprathermal electrons from the plasmasphere-RC overlap region (e.g., Khazanov et al., 1992; Gurgiolo et al., 2005). The standard collisional source

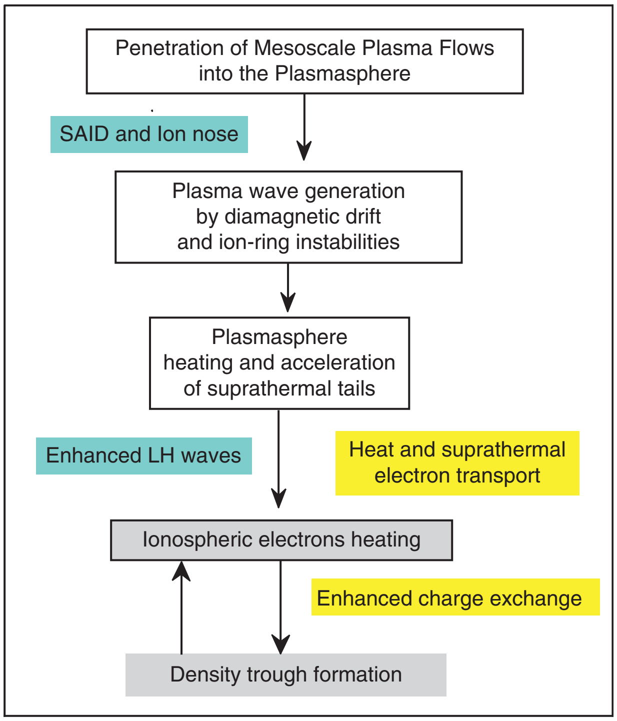

Figure 8.1 A scenario of subauroral ionospheric heating due to wave-particle interactions in the TPBL and T_e-related trough formation. Cyan (yellow) boxes indicate the resulting observables (processes).

fails to support the necessary plasmasphere's heating rate in the explored events and cannot populate enhanced suprathermal electron and ion tails. Therefore, plasmaspheric heating has been attributed to electrostatic (EIC) and electromagnetic (EMIC) ion cyclotron waves and fast magnetosonic (MS) waves generated in the RC's core (e.g., Cornwall et al., 1971; Gorbachev et al., 1992; Horne et al., 2000; Khazanov et al., 2007; Chen et al., 2010; Khazanov, 2011), as well as to lower hybrid (LH) waves near the RC inner edge (LaBelle et al., 1988; Mishin & Burke, 2005).

Figure 8.1 depicts a generic scenario of subauroral ionospheric heating (cf. Fig. 9 in Mishin et al., 2004). It includes heating and acceleration of plasmaspheric electrons due to wave-particle interactions in the TPBL, heat and suprathermal electron transport into the conjugate ionosphere, and formation of high T_e-related troughs. It is evident that the wave activity in the TPBL will shape T_e in the subauroral F region. In addition, for a given external source, ionospheric heating is facilitated inside plasma depletions (troughs). As higher temperatures result in deeper depletions, a typical positive-feedback loop, $\delta T \rightarrow |\delta n| \rightarrow \delta T$, is formed and facilitates the TGI necessary condition $\nabla_\perp n \cdot \nabla_\perp T < 0$.

Recent observations from Cluster, Van Allen Probes (RBSP), and Time History of Events and Macroscale Interactions during Substorms (THEMIS) have detailed the features of plasma turbulence in the TPBL, significantly advancing the understanding of subauroral plasma heating. This chapter surveys the key features of subauroral mesoscale and small-scale structures and their sources through an assessment of multispacecraft experiments and comparison with theoretical and numerical models. The chapter is organized as follows: The subsequent two sections outline electromagnetic and plasma structures in the plasmasphere and topside ionosphere; their formation mechanisms are discussed next. We do not dwell on theoretical and simulation details but describe only semiqualitative basic features, just sufficient for understanding experimental results. Details and rigorous derivations, as well as relevant statistical results, can be found in the referenced original papers and reviews.

8.2. TURBULENT PLASMASPHERE BOUNDARY LAYER

We begin with the basic features of the TPBL in the premidnight sector. Figure 8.2 shows the data from various spacecraft during individual substorms on 18 March 2002 ($AE \approx 300$ nT, the onset at $t_{eo} \approx 09{:}50$ UT) and 8 April 2004 ($AE \approx 600$ nT, $t_{eo} \approx 06{:}10$ UT) (Puhl-Quinn et al., 2007; Mishin & Puhl-Quinn, 2007; Mishin et al., 2010) and the main phase of the St. Patrick's Day 2013 storm (Mishin et al., 2017) that started at $t_{eo} \approx 09{:}40$ UT with the expansion of the fourth consecutive substorm. The Cluster (C1–C4) and RBSP-B spacecraft detected Southern Hemisphere SAID of the width $\Delta_s \approx 0.1R_E$ and peak electric field $E_s \approx 10$ (2002), 25 (2004), and 35 mV/m near $L = 4.9$, 4.1, and 3.1 at 23.1, 21.9, and 21.4 MLT, respectively. C1–C4 satellites had the maximum separations of 300 (18 March 2002) and 1,000 (8 April 2004) km and observed virtually the same parameters of the SAID channels in both hemispheres. Polar was magnetically conjugate to Cluster in the Northern Hemisphere.

The SAID channel with the wave "burst" is interior to the PS boundary/plasmapause in the substorm events but centered on it in the midst of the storm. A probable cause of the latter is the plasmasphere's erosion inside the channel (e.g., Goldstein et al., 2003; Huba et al., 2017), which is negligible near substorm onsets. The 2004 and 2013 events have the wave spectra more enhanced not only near the PS boundary but also farther inward than in the 2002 event. It is consistent with the greater SAID peaks and ion fluxes and energies, as the SAID field is determined mainly by the hot ion pressure gradient (Mishin &

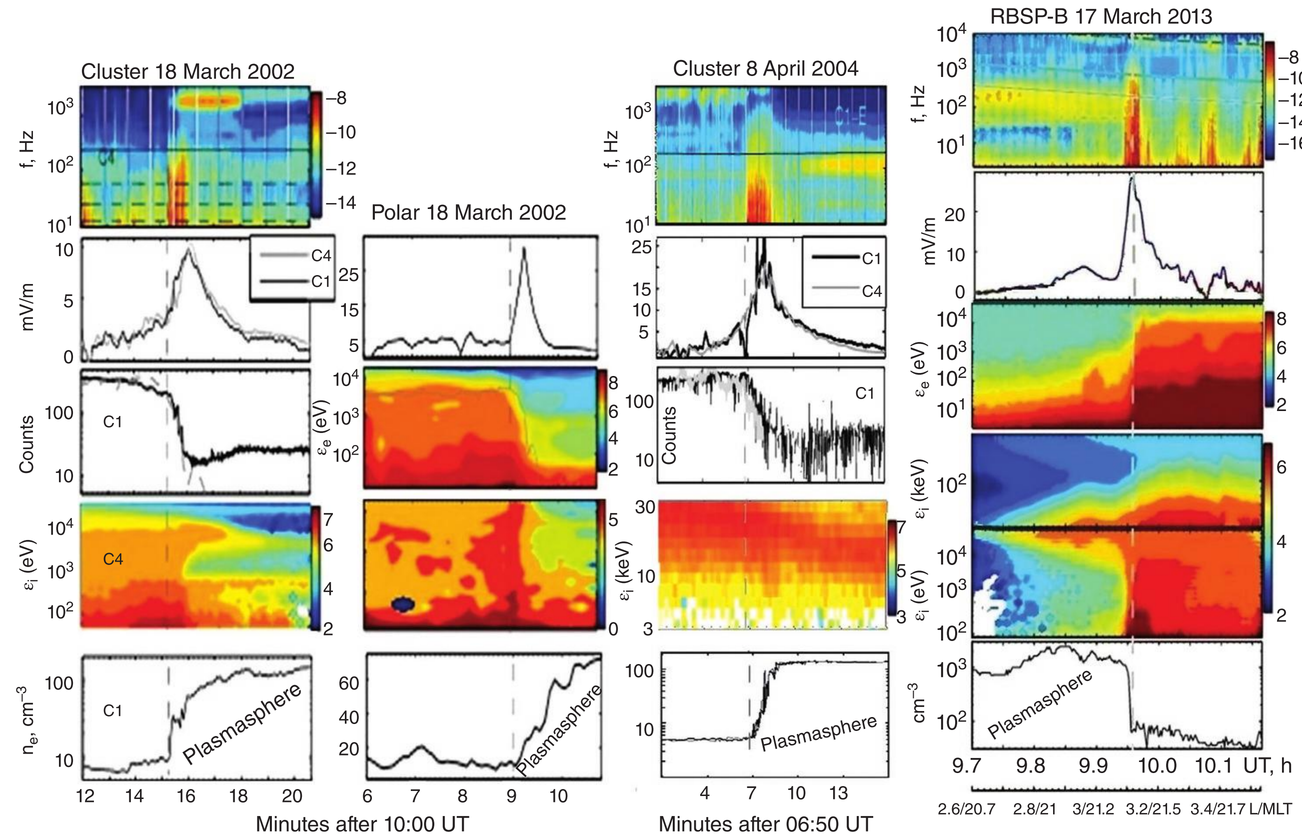

Figure 8.2 (Top row) Frequency-time spectrograms for the electric fields in (V/m)^2/Hz (the dark solid thick/thin line indicates the H$^+$/O$^+$ lower hybrid resonance ($f_{lhr}/f_{lhr}^{(O)}$) and dashed lines indicate the second, fourth, and tenth harmonics of the proton gyrofrequency (f_{ci}); (Second) meridional (outward) electric fields; (Third) C1 1-keV electron counts and omnidirectional electron fluxes from Polar, with the scaled F14 1-keV electron flux (the grey line), and RBSP-B; (Fourth) H$^+$ differential number fluxes from C4 ($\perp\mathbf{B}_0$) and Polar (omnidirectional) in (cm^2 s sr keV)$^{-1}$ and differential energy flux from RBSP-B; (Bottom) the plasma density. Color codes for the wave spectra and particle fluxes are in logarithmic scale. Ephemeris data are shown in the bottom. The vertical dashed line indicates the PS boundary (after Puhl-Quinn et al., 2007, and Mishin et al., 2010, 2017).

Puhl-Quinn, 2007) that, in turn, drives the ion diamagnetic drift current near the inner edge.

Figure 8.3 shows the second-order quantities including the root-mean-square (rms) electric field from Cluster and RBSP-B, $\delta E = \sqrt{\sum \Delta f \cdot \delta E_f^2}$ for LH (at $f_{lhr} \le f_{lh} \le 3f_{lhr}$), MS ($f_{ci} < f_{ms} < f_{lhr}$), EMIC ($f_{emic} < f_{ci}$), and lower hybrid oblique resonance (LOR, $f_{lor} > 5f_{lhr}$) waves, and δE_f from Polar at f = 32, 256 ($\approx 20f_{ci}$), and 2,048 ($\approx 2f_{lhr}$) Hz; the hot electron and ion (H$^+$ and O$^+$) pressure with the H$^+$ anisotropy ($\delta T_p = T_\perp/T_p - 1$); and azimuthal currents calculated from the measured onboard magnetic field. Here f_{lhr} is the lower hybrid resonance and f_{ci} is the ion cyclotron frequency.

The presence of a narrow peak in the hot electron pressure, P_e (and the density, N_e), near the PS boundary is apparent in the Polar and RBSP-B data (frames (e)–(f)). In addition, we show the THEMIS-A/B/D hot electron and ion pressure radial profiles (Fig. 5 in Mishin & Sotnikov, 2017) obtained during successive crossings of the plasmapause/PS boundary by the THEMIS spacecraft following two substorms commencing at 11:15 and 14:25 UT on 23 March 2007. At ≈15:30 (16:30) UT, TH-D, followed by TH-B and A in ~10-min succession, encountered the PS boundary (5 keV electron cutoff) near L = 6.5 and 21.6 MLT and the ion inner edge (nose) near L = 4.5 and 22.7 MLT (Fig. 2 in Runov et al., 2008). Such pressure peaks are created by the inflowing MPF's electrons near the stopping point at the plasmapause (Mishin et al., 2010, 2017). As shown in the THEMIS data, this peak decays in about 1.5 hours after the substorm onset, while that of the hot (ring current) ions persists for, at least, ~5 hours. The P_e-peak drives a pair of oppositely directed, azimuthal diamagnetic drift currents with the drift speed $u_d = -\varkappa_e \omega_{ce} r_{ce}^2$,

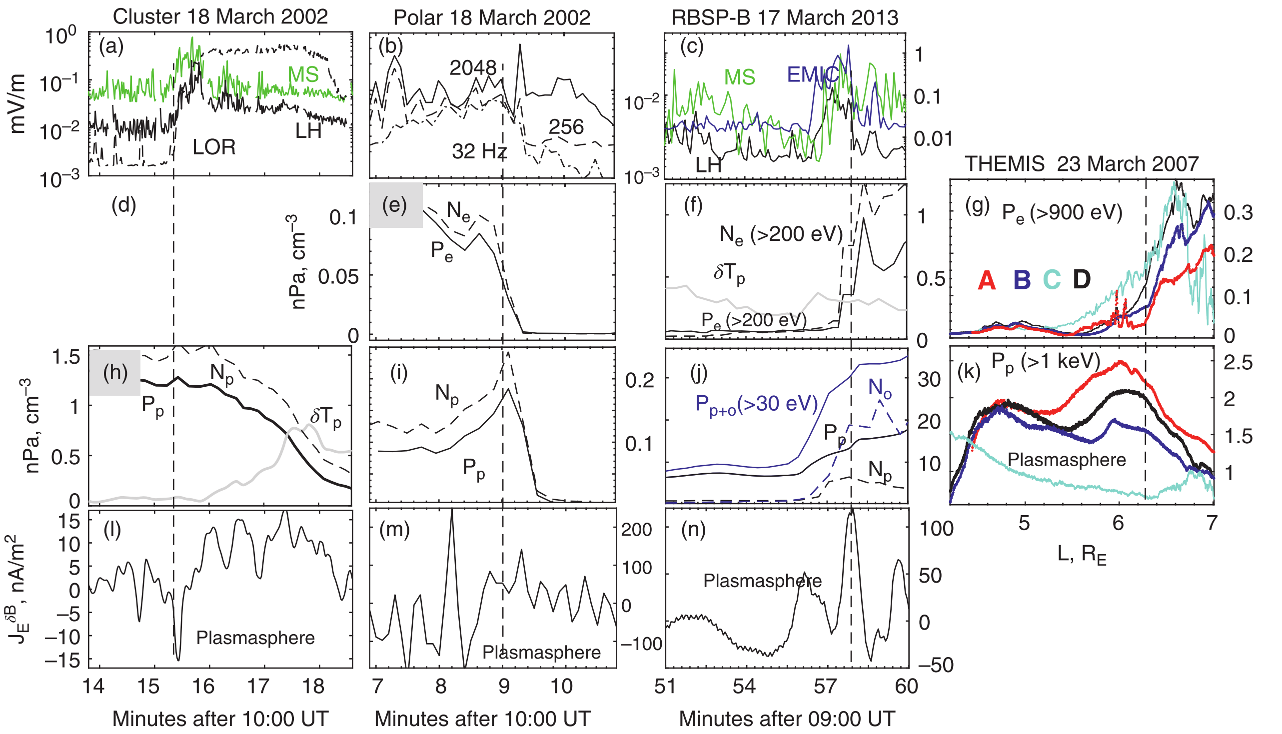

Figure 8.3 (a)–(c) The r.m.s. amplitude of wave electric fields δE_{lh} (solid black), δE_{ms} (green), δE_{emic} (red), δE_{lor} (dashed), and δE_f at f = 32, 256, and 2048 Hz; (e)–(g) perpendicular electron pressure P_e; (h)–(k) perpendicular pressure of H^+ ions at (h) C4, (i) Polar, and (k) THEMIS, and (j) H^+ and $H^+ + O^+$ ions at RBSP-B; and (l)–(n) azimuthal currents (positive eastward). Vertical dashed lines indicate the PS boundary. δT_p is the hot ion anisotropy (see text) (after Mishin, 2013, and Mishin & Sotnikov, 2017).

where $\varkappa_e = \dfrac{d}{dr} \ln P_e$. The eastward current is inward of the westward counterpart located exterior to or at the PS boundary, which is consistent with the observed pattern near the PS boundary (frames (l)–(n)). Quite similar current structure is also observed on 8 April 2004 (Fig. 3 in Mishin & Puhl-Quinn, 2007).

Inward of the entry layer, the only source of free energy for plasma waves is the hot (RC) ion population. The ion temperature anisotropy δT_p increases toward the inner edge (tip), and the energy dispersion, $\delta\varepsilon_\perp \approx \delta\varepsilon = \varepsilon_{\max}/\varepsilon_{\min} - 1$, decreases. Thus, the anisotropic ion distribution approaches an ion ring in the energy range $\varepsilon_{\min} \le \varepsilon \le \varepsilon_{\max}$

$$f_h(v_\perp) \approx \frac{N_h}{\pi v_{Tr}^2} \exp\left(- \frac{(v_\perp - v_r)^2}{v_{Tr}^2} \right), \tag{8.2}$$

with $m_i v_r^2 = \varepsilon_r \approx \varepsilon_{\max}\left(1 - \frac{1}{2}\delta\varepsilon\right)$ and $m_i v_{Tr}^2/\varepsilon_{\max} = \delta\varepsilon$. The anisotropic ion instability is typically considered as the main excitation mechanism in the ring current (e.g., Horne et al., 2000; Khazanov et al., 2007; Mithaiwala et al., 2010; Khazanov, 2011). In the RBSP-B event, both the H^+ and O^+ (not shown) ion rings are present.

As a rule of thumb, an ion ring can excite MS waves at $\omega \ge 30\omega_{ci}$ when the mean ion-ring speed v_r exceeds the Alfvén speed v_A,

$$v_r > v_A(n_c) \quad \text{or} \quad n_c > n_A \approx \frac{25}{\varepsilon_r(\mathrm{keV})}\left(\frac{B_0(\mathrm{nT})}{100}\right)^2 (\mathrm{cm}^{-3}), \tag{8.3}$$

and at $\omega < 30\omega_{ci}$ when $v_R > 2v_A$ (e.g., Horne et al., 2000). In the substorm events, the condition (8.3) becomes valid only near the channel's center. In the storm-time entry layer, with $n_c > n_A$, the dispersion is too large ($\delta\varepsilon \sim 1$) and anisotropy is too small ($\delta T_p \sim 0.1$) for the ion ring instability to develop. Therefore, the intense waves in the entry layer are driven mainly by the electron diamagnetic currents, while, near the tip, both the ion ring and diamagnetic drift current contribute to the excitation of a broadband wave spectrum.

Mishin (2013) and Mishin and Burke (2005) have considered the effect of nonlinear interactions of plasma particles with LH waves driven by the electron and ion diamagnetic currents in the entry layer and near the ion tip, respectively. The estimated heating rates suffice to increase the bulk plasma temperature and enhanced

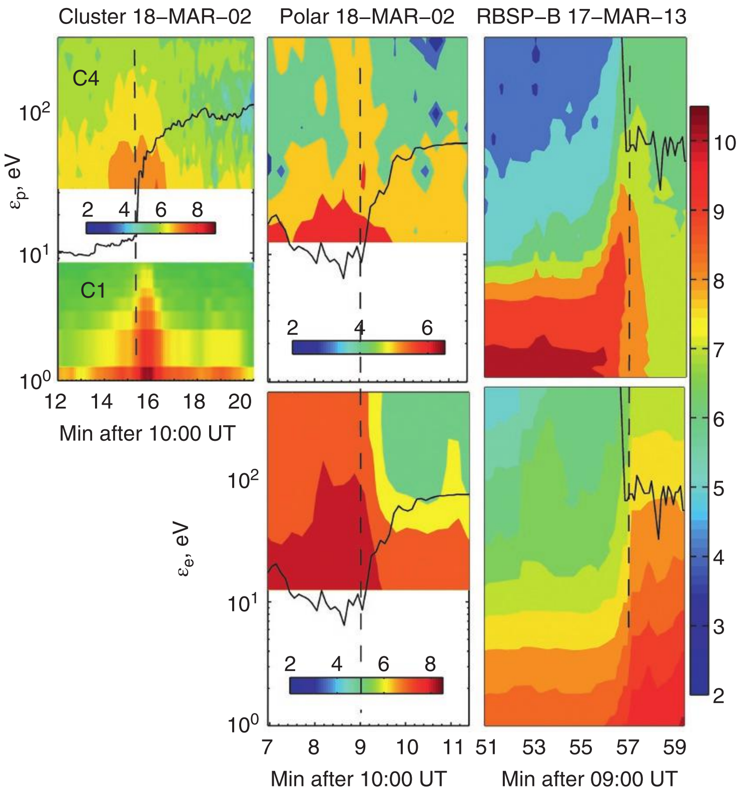

Figure 8.4 Cluster, Polar, and RBSP-B 1-500 eV (top) H^+ and (bottom) electron fluxes with the cold plasma density superimposed. Color codes are in logarithmic scale.

suprathermal, tens to hundreds eV, particles to form the "hot zones" in these regions (see the Appendix to this chapter). These are clearly seen in Figure 8.4 near and interior to the plasmapause (the O^+ thermal and suprathermal populations from RBSP-B is like that of H^+). Notably, the energy flux of suprathermal electrons reaches a few 10^{10} eV/cm^{2}s, which is sufficient for heating ionospheric electrons to ≥6000 K (e.g., Khazanov et al., 1992, Table 2).

So far, we considered premidnight narrow-width SAID events. Duskside broad TPBL are exemplified by two SAPSWS events in Figure 8.5 encountered by the RBSP-A probe at about -12° MLat off the magnetic equator during the 17 March 2015 storm (Mishin et al., 2017; Mishin & Sotnikov, 2017). The first one was crossed between L = 4.4–4.7 and 20.2–20.5 MLT shortly after the onset of a substorm at 07:00 UT at the very beginning of the storm. The second crossing between L = 2.8–3.4 and 17.5–18.1 MLT occurred during the main phase of the storm with multiple substorm activations initiated by the arrival of a series of ~20–35 nPa solar-wind ram pressure pulses at ≈13:00 UT (e.g., Jacobsen & Andalsvik, 2016). Notably, irregular fields are continuous around the PS boundary, and the E_H and E_V components mirroring each other ($e_V = e_r$ (radial/outward), $e_D = e_\varphi$ (azimuthal/eastward), and $e_H = -e_\theta$ (meridional/northward)). This means that the satellite travels through a two-dimensional (2-D) structure localized in the radial direction and extended in the azimuthal direction.

Besides the dominance of oxygen ions (cf. Burke et al., 2016) and shifting inward in the subsequent crossings, small-scale oscillations weaken (cf. Mishin & Burke, 2005) and the spectra of plasma waves and suprathermal particles differ significantly across the channel. The ion population during the first crossing is dominated by ~3–30 keV protons with the energy dispersion $\Delta\varepsilon_\perp/\varepsilon_{\min} \sim 1$ and anisotropy $\Delta P/P_p$ (not shown) ~0.1 inside the channel. However, the dispersion inward of the channel dropped to ~0.2, while the anisotropy increased to ~0.3. The storm main phase is dominated by oxygen ions, likewise the RBSP-B 17 March 2013 SAID event. The energy dispersion of both O^+ ions and protons decreases across the channel from $\Delta\varepsilon_\perp/\varepsilon_\perp \sim 0.3$ to ~0.1–0.2, while the anisotropy increases from ~0.1–0.2 to ~1. That is, their distributions can also be approximated by the distribution (8.2).

The wave activity in the PS is weaker in the main-phase event due to a less energetic and more isotropic electron population but stronger inside and inward of the channel, especially the electromagnetic component (Fig. 6 in

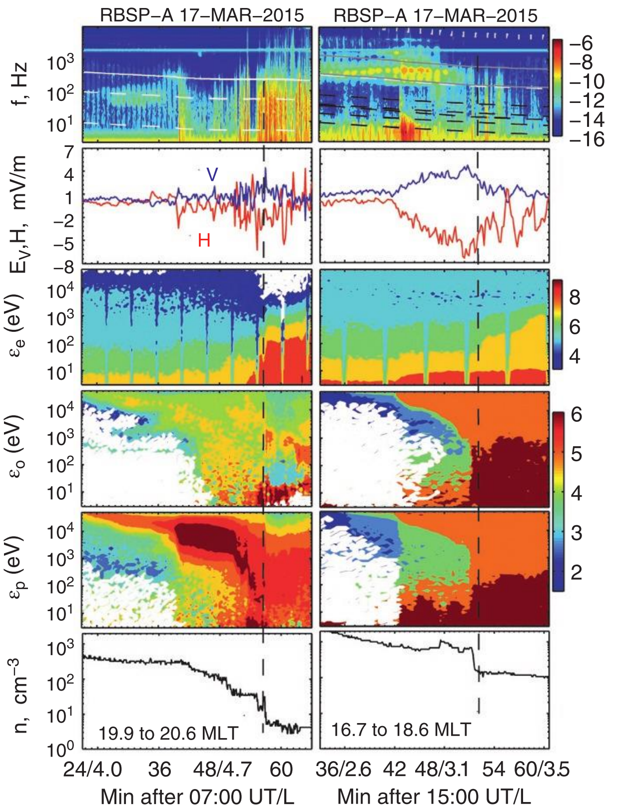

Figure 8.5 SAPSWS detecteds by RBSP-A on 17 March 2015. The same format as Figure 8.2 but with addition of the O^+ ion fluxes (after Mishin et al., 2017, and Mishin & Sotnikov, 2017).

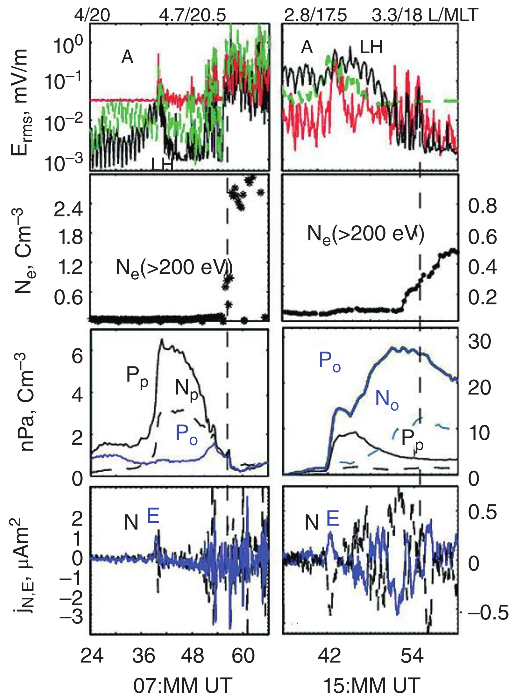

Figure 8.6 The rms amplitude of wave electric fields (δE_{lh} (solid black), δE_{ms} (green), δE_{emic} (red)), hot electron density, perpendicular ion pressure, and azimuthal and field-aligned currents in the region of SAPSWS in Figure 8.5. The same format as Figure 8.3 (after Mishin & Sotnikov, 2017. Reproduced with permission of IOP Publishing).

Mishin & Sotnikov, 2017, Figure 6). It is seen in Figure 8.6 that the wave bursts near the boundaries collocate with azimuthal and field-aligned currents. The oscillatory currents near the PS boundary are mainly related to tens of mHz compressional and shear MHD (Alfvén) modes (cf. Mishin et al., 2003; Streltsov & Mishin, 2003; Streltsov & Foster, 2004; Mishin & Burke, 2005). Here, the electron and ion diamagnetic drift currents contribute notably only during the expansion phase, which is consistent with the ion "hot zone" like Figure 8.4. On the other hand, likewise Figure 8.3, the wave activity near the TPBL inner boundary is dominated by the ion diamagnetic drift current (cf. Figs. 3 and 14 in Mishin & Burke, 2005).

The role of the the anisotropic ion (ring) instability is manifested by the significant difference between the LH/MS wave amplitudes in the center of the channels. Namely, the low amplitudes correspond to a small anisotropy and broad energy distribution (large dispersion). In addition to the RBSP-A crossings, RBSP-B encountered SAPSWS near -19° MLat (not shown) after the substorm recovery, just before the main phase commencement. In this event, the hot electron pressure was greatly reduced, but the amplitude of EMIC waves in the center was about the same as during the substorm expansion, that is, $\delta E_{emic} \approx 0.02$ mV/m. Probably, this indicates the excitation by the core ring current (e.g., Khazanov et al., 2003). Overall, the wave power as well as the plasma sheet and suprathermal electron fluxes are weaker than in the SAID events.

In summary, there are three principal sources of free energy for plasma waves in the plasmasphere boundary layer. Those include the electron and ion diamagnetic drift currents due to the corresponding pressure gradients and the anisotropic ion distribution. Their relative contributions vary in the course of storms, and even at different substorm phases, and differ between premidnight and duskside events. The spatial structure of the enhanced wave activity and concomitant plasma temperature and suprathermal particles in the TPBL change accordingly. Similar changes occur in ionospheric density and temperature structures, which are discussed next.

A general remark is in order. In the events under consideration, we do not have access to the F region where the charge exchange process takes place. In general, the trough relative depth,

$$\delta n_m = 1 - \frac{n_{\min}}{n_0}; \quad \delta n_m \to 1 \text{ at } n_{\min} \to 0 \qquad (8.4)$$

(n_{min}/n_0 is the minimum/background density), in the topside and F-region ionosphere can differ significantly (e.g., Anderson et al., 1991). In particular, plasma outflows deplete the F region, while increasing the topside density. On the other hand, a steady-state density profile is in diffusive equilibrium with a given temperature profile (Schunk et al., 1976). The F-region electron temperature in similar SAPS events was only a factor of 1.5–2 smaller than on topside (e.g., Fig. 6b in Foster et al., 1994; Figs. 5b and 6 in Förster et al., 1999). The O^+ scale height in high-temperature events is as large as 300–500 km, so nearly a flat altitude profile, $\delta n_m(h) \approx$ const, from the bottom to the top of the trough should be eventually established (cf. Fig. 6c in Foster et al., 1994). This makes the DMSP measurements of δn_m a reasonable proxy for the disturbed F-region trough.

8.3. IONOSPHERIC STRUCTURES

On average, on large scales, storm-time ionospheric density troughs coincide with SAPS and SAID and collocate with the elevated temperature (e.g., Foster et al., 1994; Moffet et al., 1998; Foster & Vo, 2002; Prölls, 2006). However, at smaller scales, this relation is frequently violated in individual events and changes with time (e.g., Figueiredo et al., 2004). As an example, Figure 8.7 shows the ionospheric temperature and density

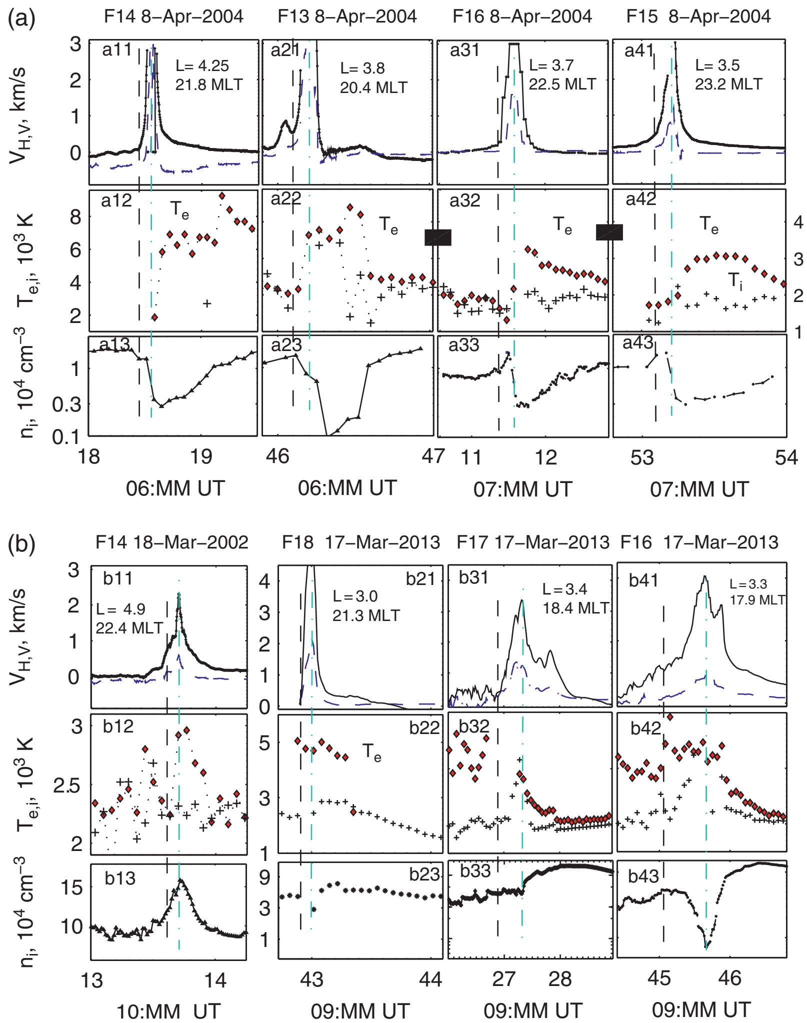

Figure 8.7 Ionospheric structures during the SAID events on (a) 8 April 2004 and (b) 18 March 2002 and 17 March 2013. (Top row) The horizontal (black lines) and vertical (dashed blue) components of the drift velocity; (second row) the electron (red diamonds) and ion (crosses) temperature; and (third row) the plasma density. Black boxes connect frames with the same scale of the y axes. The dashed (cyan dash-dot) line indicates the PS boundary (SAID peak).

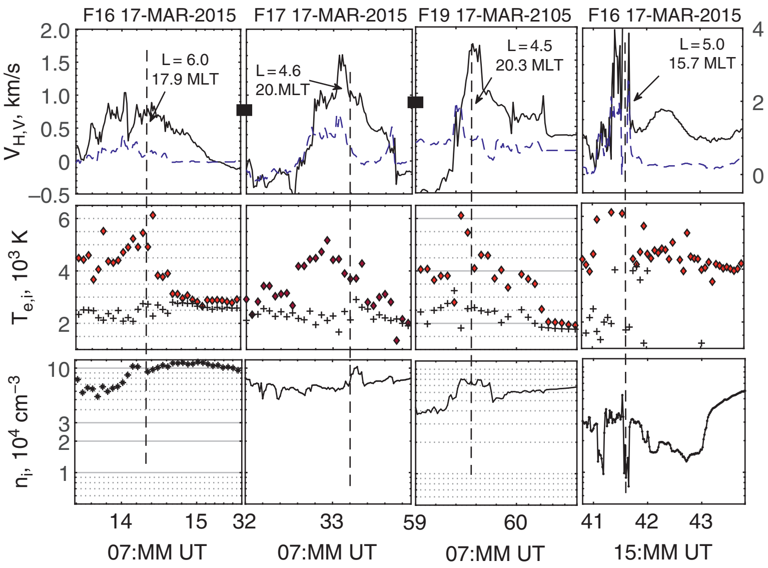

Figure 8.8 Ionospheric structures during the 17 March 2015 SAPSWS events. The same format as Figure 8.7.

variations related to the SAID events in Figure 8.2. The electron temperature is elevated largely inside the SAID channel in the F14/2002 event (frame b12) and also extends outside the channel in the 2004 (frames a12–a42) and 2013 (frames b22–b42) events. This is consistent with the difference between the TPBL wave activities in these events, as discussed earlier with Figure 8.2. According to the subauroral ionospheric heating scenario (Fig. 8.1), heating and acceleration of plasmaspheric electrons in the TPBL enhances the heat and suprathermal electron fluxes, thus leading to elevated T_e at the foot point in the ionosphere.

As consistent with the trough-plasmapause statistical relation (e.g., Yizengaw & Moldwin, 2005) and the short-circuiting scenario (Mishin & Puhl-Quinn, 2007; Mishin, 2013), the 8 April 2004 SAID are located on the trough's poleward wall, which changes with time under the action of the SAID electric field, $E\left(\frac{\text{mV}}{\text{m}}\right) \approx 38 \cdot V_H\left(\frac{\text{km}}{\text{s}}\right)$, and upward flows. The equatorward wall appears to be impacted by the elevated T_e that decreases with time, especially near the auroral boundary. The latter implies the declining TPBL wave activity during the substorm recovery, particularly in the entry layer where the decaying electron pressure peak is the major driver.

In addition to the premidnight SAID from F18 during the 17 March 2013 storm, multiple SAPS channels were detected on the duskside. In particular, F17 and F16 encountered the same flow channel before and after the start of the storm main phase (cf. Fig. 8.5 in Mishin et al., 2017). The obvious structural difference between the F17 and F16 density profiles is the density trough in the SAPS region consequent to the combined effect of the enhanced electric field and electron temperature.

Figure 8.8 presents some of the ionospheric structures in the Southern Hemisphere, almost coincident with the SAPWS on 17 March 2015 (Fig. 8.5). Overall, the average magnetospheric and ionospheric patterns map fairly well but small-scale ionospheric features are much less pronounced. Similar to the SAID events, the wave activity in the plasmasphere (Fig. 8.6) correlates with the electron temperature. It decreased near the PS boundary in ~30 minutes after the substorm onset and increased near the inner edge in contrast with the decrease of the plasma density. The density profile during the storm main phase becomes highly irregular and depleted, on average mirroring the plasma drift and temperature.

Figure 8.9 exemplifies strong SAPSWS detected during storm-time substorms on 6 April 2000 and 6 November 2001 (Mishin et al., 2003, 2004). As usual (Mishin & Burke, 2005), they correlate with precipitating freshly injected RC ions (not shown), elevated electron temperatures, and broad irregular plasma density troughs. The troughs' equatorward part coincides with the elevated T_e up to $(7-9) \cdot 10^3$ K and is displaced by ~100 km from the oscillatory pattern coincident with precipitating RC ions and ion outflows. In order to avoid the contribution of the enhanced electric fields, precipitating ions, and upward flows, only data acquired in the equatorward part are used to explore effects of electron heating.

It is instructive to study how the relative plasma density, $\delta n_i/n_0 = 1 - n_i/n_0$, varies with the mean ion energy in the center of mass system of interacting O^+ and N_2 (or O_2),

$$\varepsilon_{i-n} \approx T_i + \frac{1}{2}T_n + \frac{m_i v_d^2}{3\kappa}. \tag{8.5}$$

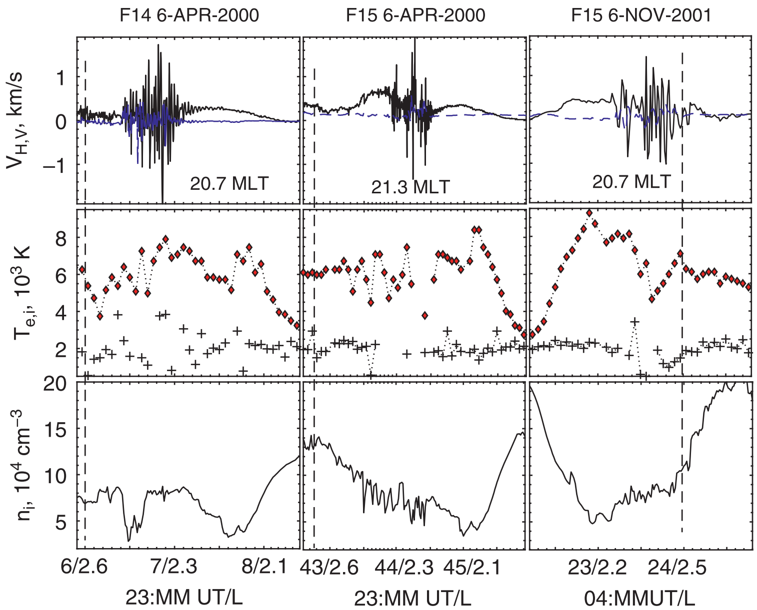

Figure 8.9 Storm-time strong SAPSWS observed by DMSP F14 and F15 on 6 April 2000 and 6 November 2001, respectively. The same format as above.

Here n_0 stands for the plasma density at the equatorward edge of the events, $v_d = c\,E_0/B_0$ is the plasma drift speed, and κ is the Boltzmann constant. As usual, the effective ion temperature is defined as $T_{i-n} = \frac{2}{3}\varepsilon_{i-n}$. For simplicity, we take $m_n \approx 2m_i$ and $T_n = 1000$ K.

Figure 8.10 shows δn_i-variations along the satellite track versus coincident ε_{i-n} and T_e obtained in five SAPSWS events. Here "XX/YY" designates events encountered by the DMSP FXX satellite near YY UT during the 6 April storm, while "Nov6" stands for the F15 6 November 2001 event in Figure 8.9. In general, δn_i appears to be independent of ε_{i-n} but increases almost linearly with T_e until saturation at $\delta n_m \approx 0.8$ for $T_e \geq 6000$ K (Mishin et al., 2004).

Let us turn to consider short-scale irregularities within the SAPSWS close to the regions of strong midlatitude UHF (Basu et al., 2001) and GPS (Ledvina et al., 2002) storm-time scintillations on 22 September 1999 and 26 September 2001, respectively (Mishin & Blaunstein, 2008). Each SAPSWS event was observed by a pair of the DMSP satellites, F13 and F14. The waveforms of relative density variations, $\delta n/n$, in the frequency range of 1–10 Hz (bottom frames) emphasize their oscillatory character. The upper frequency cutoff is defined by the sampling rate of 24 Hz. Unfortunately, gaps in the temperature data coincident with strong irregularities prevent analysis of any mutual interrelation.

Given the satellite speed $v_{sat} = 7.5$ km/s, apparent frequencies $f_a = 1$–10 Hz correspond to the apparent wavelengths $\lambda_a = v_{sat}/f_a \approx 0.75$–$7.5$ km along the satellite track.

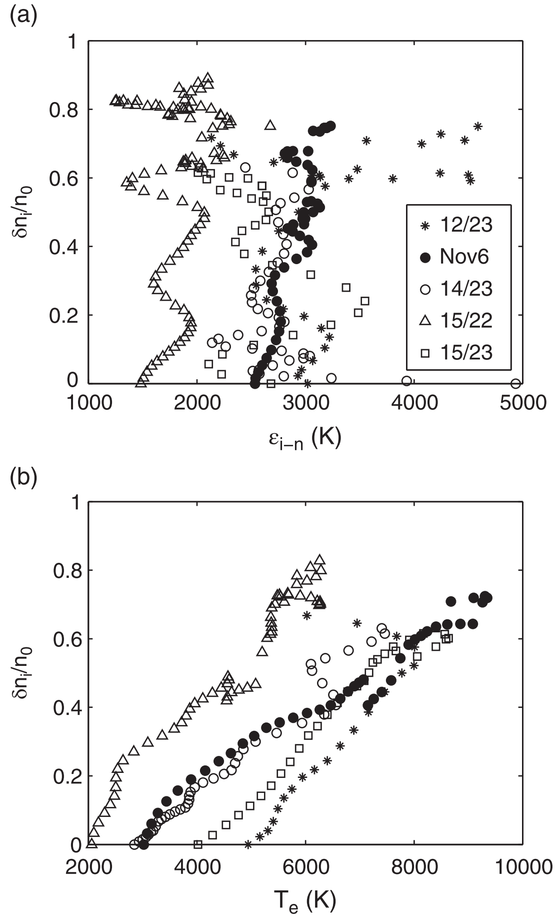

Figure 8.10 Variation of the relative plasma density with (a) ε_{i-n} and (b) T_e in five events studied (see text).

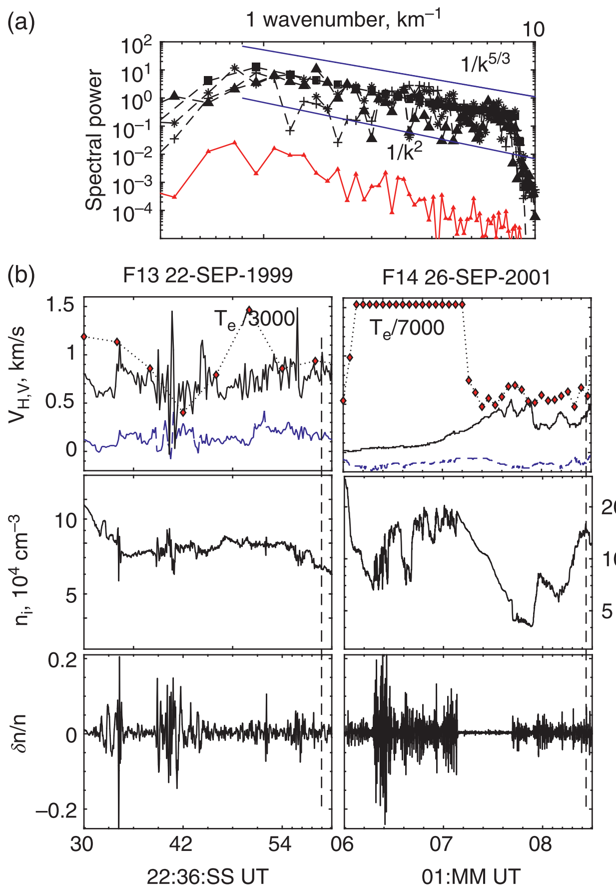

Figure 8.11 (a) The spectral power of plasma irregularities during the scintillation events and inside an average "quiet-time" SAPS-related trough (the red line) as a function of spatial wavenumber. (b) From top to bottom: The westward and vertical components of the convection velocity with the scaled T_e superimosed, density variations along the satellite tracks, and waveforms of relative density variations in the frequency range 0.1–9.5 Hz (after Mishin & Blaunstein, 2008. Reproduced with permission of John Wiley and Sons).

This implies the satellite crossing time is much shorter than the actual wave period. The storm- time spectra in Figure 8.11a are represented by a power law $(\delta n_k/n_0)^2 \propto k^{-p_n}$ with the spectral index $5/3 < p_n \leq 2$ in the range $10 > k_a \geq 0.8$ km^{-1} (cf. Fig. 9 in Foster & Rich, 1998). It is evident that the storm-time irregularities greatly exceed the quiet-time level, even in the short scales ($\lambda_a \leq 800$ m) that are cut off due to the sampling rate. As noted in the Introduction, during similar events, enhanced decameter-scale irregularities are revealed in the high-resolution measurements on board DEMETER and routinely detected by the SuperDARN radars.

To summarize, a great variety of mesoscale and small-scale structures, ranging from a few degrees in latitude down to a fraction of a meter, are present in the disturbed subauroral ionosphere. We discuss their generation mechanisms in turn from larger to smaller scale lengths, that is, starting with subauroral troughs, next SAPSWS, and then decameter-scale irregularities.

8.4. DISCUSSION

8.4.1. Subauroral Density Trough

The ionization balance in the O^+-dominated F region is determined by the recombination of NO^+ and O_2^+ created via charge exchange, equation (8.1), since the recombination rate of O^+ ions is very small. Thus, the formation of SAPS/SAID-related troughs has long been explained through a combination of enhanced recombination stemming mainly from the reaction (8.1) and plasma outflows due to frictional ion heating (Schunk et al., 1976; Anderson et al., 1991; Moffet et al., 1998). This is easily understood from the dependence of the charge exchange rate on the ion temperature, drift speed, and vibrational states,

$$k_1 = k_{1,0}\left(\left(N_2^{(0)}\right) + \sum_{V\geq 1} c_V \cdot \left(N_2^{(V)}\right)\right). \tag{8.6}$$

Here $k_{1,\,0}$ is the ground-state rate coefficient, $(N_2^{(V)})$ is the density of the V-vibrational state of N_2, and $c_V = k_1^{(V)}/k_1^{(0)}\Big|_{300\mathrm{K}}$ are the specific rate coefficients established within the experimental uncertainty~20% (see Viggiano & Williams, 2001, for details). Since at $T_i \geq 1800$ K, the effects of vibrational excitations are more significant for k_1 and the density ratio in the F-region ionosphere $(N_2)/(O_2) \sim 10$, to first order, one needs only to account for the charge exchange with N_2.

Figure 8.12 shows analytical approximations for k_1 derived from the high-temperature flowing afterglow (HTFA) experiments for Boltzmann's distribution of $N_2^{(V)}$ (Viggiano & Williams, 2001). An analytical approximation for $k_{1,\,0}(T_i)$ is obtained from the drift tube data with $\kappa T_i = T_n + \frac{1}{3\kappa} m_i v_d^2$ with $T_n \leq 300$ K (St.-Maurice & Torr, 1978). For ballpark estimates, note that electric fields ~0.1 V/m yield $\delta n_m \approx 0.7$ at ~300 km altitude (Schunk et al., 1976). These fields correspond to horizontal drift velocities $v_H = v_d \sim 2$ km/s and $T_i \sim 3700$ K for $T_n = 1000$ K. From Figure 8.12, one gets $k_{1,0}(T_i = 3700) \approx k_1(T_i \approx 1700, T_V = 3000)$.

Figure 8.13 represents the results of numerical calculations of the T_e-related trough formation in the local approximation for the typical midlatitude parameters of neutral gas at 300 km (Mishin et al., 2004). Besides reaction 8.1 for NO^+ production, the variation of the vibrational population, $\eta_V = \left(N_2^{(V)}\right)/(N_2)$, and the plasma density, n_e, are described by

$$\frac{\partial}{\partial t}\eta_V = \beta_V Q_V \eta_0 - L_V \eta_V + L_O \eta_{V+1} \quad (8.7)$$

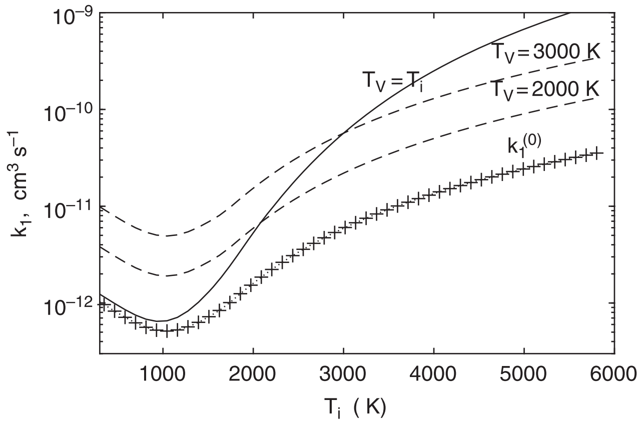

Figure 8.12 The rate coefficient for the reaction (1) with N_2: Pluses "+" show $1.2{\cdot}k_1^{(0)}$, solid and dashed lines show k_1 calculated with $k_{1,0} = 1.2{\cdot}k_1^{(0)}$, with T_V indicated.

and

$$\frac{\partial}{\partial t}n_e = k_1(0)\,n_i(0)\,(N_2) - \alpha_r\,(n_e - n_i)\,n_e. \quad (8.8)$$

Here Q_V is the production and L_V is the loss rate of vibrational levels, $n_i = (O^+)$, and $\alpha_r \approx 4{\cdot}10^{-7}\left(\frac{300}{T_e}\right)^{0.5}$ $cm^{-3}s^{-1}$ is the recombination rate of NO^+ ions; $n_i(0)$ is taken equal to $n_e(0)$ as the initial condition, and $n_e(t) = n_i(t) + (NO^+)(t)$.

Figure 8.13a shows the total relative rate, Q/n_e, of vibrational excitation by thermal (Maxwellian) electrons as a function of T_e, with the branching ratios $\beta_V \sim 0.6$, 0.3, 0.1, and 0.05 for $V = 1$, 2, 3, and 4 at $T_e \geq 2000$ K, respectively. The contribution of suprathermal electrons via electronic triplet states is neglected. At altitudes ~300 km, the main quencher of vibrational states is atomic oxygen with the rate coefficient $L_O/(O) \approx 10^{-10}{\cdot}\exp\left(-70/T_n^{1/3}\right)$ s^{-1}, where (O) is the atomic oxygen density. Accounting for charge transfer yields $L_V = L_O + c_V{\cdot}k_1^{(0)}{\cdot}n_i s^{-1}$. The vibrational distribution is far from equilibrium, as the $V-V$ exchange rate is insignificant at altitudes ~300 km. To evaluate k_1, the population of the first five states was calculated, assuming $\eta_{V\geq 5} = 0$. Figure 8.13b shows the ratio $k_1/k_{1,0}$ versus time, calculated at $T_i = 2000$ K with various

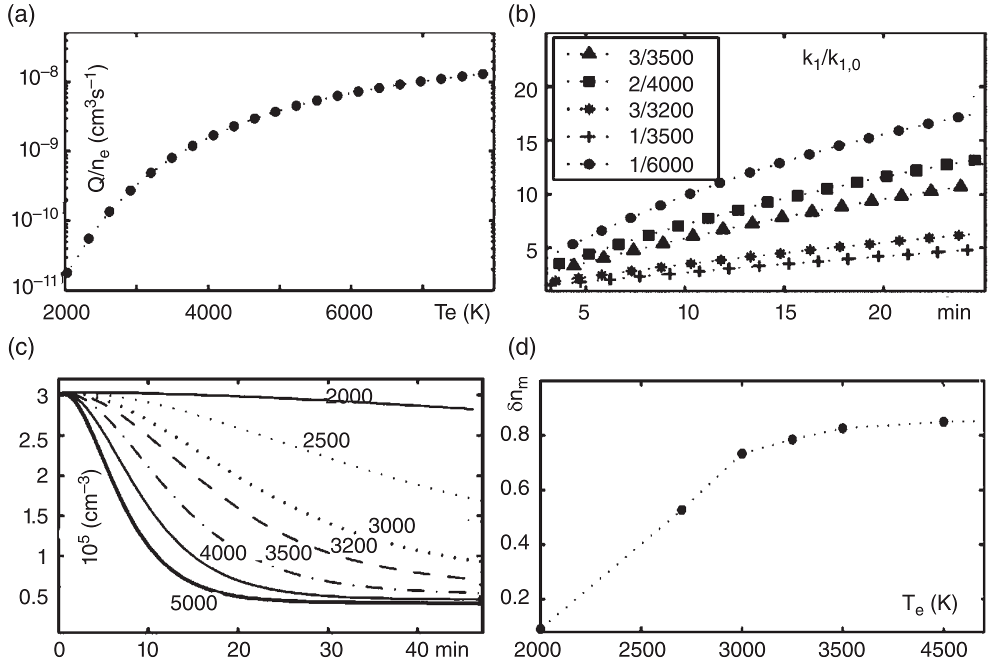

Figure 8.13 (a) Rate coefficient for the vibrational excitation ($V = 0 \rightarrow V > 0$) of N_2 by thermal electrons; (b) variation of the $k_1/k_1^{(0)}$-ratio with time calculated at $T_i = 2000$ K with various combinations between $T_e \approx 3200$, 3500, 4000, or 6000 K and n_e=(1, 2, 3)$\cdot 10^5$ cm^{-3}, designated in label; (c) variation of the plasma density with time at 300 km for T_e=2000, … 5000 K; $T_i = 2000$ K; (d) variation of the trough depth at the end of run as a function of T_e (after Mishin et al., 2004).

combinations between T_e and n_e indicated (e.g., 3/3500 means $n_e = 3 \cdot 10^5$ cm^{-3} and $T_e \approx 3500$ K). The production of NO^+ intensifies in about 5 to10 min. As the recombination rate of NO^+ ions is less than 1/min for $n_e \geq 10^5$ cm^{-3}, the depletion rate is of the order of $\tau_d^{-1} \sim k_1(N_2)$.

Figure 8.13c shows the variation of the plasma density at ~300 km with time for $T_i = 2000$ K and $T_e = 2000 - 5000$ K. Clearly, the plasma density decreases by a factor of about 5 or $\delta n_m \approx 0.8$ in 10 to 15 min. The relative density depletion at the end of run versus T_e is plotted in Figure 8.13d. As T_e on the topside is greater than in the F region by a factor of 1.5 to 2, the δn_m-vs.-T_e dependence is consistent with that in Figure 8.10b. Note that the decrease of the electron density for a given electron heating source leads to higher electron temperatures that provide higher excitation rates and thus shorter decay times. This effect was not included. The gain in T_e rapidly decreases below 300 km (e.g., Foster et al., 1994), along with the number of "vibrationally active" electrons in the high-energy tail at $n_e/(N_2)$ under $\sim 10^{-3}$ (Mishin et al., 2000). Both factors make the vibrational mechanism inefficent below ~250 km. Finally, the presumption of the heating source persistence longer than τ_d may not be valid during fast expansion of the auroral zone in strong substorms.

The local approximation is violated at altitudes above ~400 km as the rate of ambipolar diffusion exceeds the depletion rate. The depletion process proceeds as follows (no horizontal diffusion is involved): While the F-peak density decreases and the initial equilibrium breaks down, the surrounding plasma flows into the depleted region to restore the force balance. This response resembles a rarefaction wave propagating from the F peak with the characteristic time of the order of $\tau_s \sim H_{O^+}/c_s \sim$ 5–10 min, where $c_s \approx \sqrt{\kappa(T_e + T_i)/m_i}$ is the ion sound speed. Steady-state topside density profiles can be evaluated assuming diffusive equilibrium in a given temperature profile (Schunk et al., 1976). The O^+ scale height is $H_{O^+} \approx \kappa(T_e + T_i)/(m_i g_p)$. Here g_p is the field-aligned component of gravitational acceleration and m_i is the ion mass. In the events under consideration, one gets $H_{O^+} \sim$ 400–500 km. Thus, nearly constant density versus height profiles should be established, yielding $\delta n_m \approx$ const from the bottom to the top of the trough (cf. Foster et al., 1994).

8.4.2. SAPS Wave Structures

The SAPSWS generation mechanism is not completely understood. As suggested by Mishin et al. (2017), because the electric field in the subauroral part of the SCW meridional current greatly exceeds its auroral counterpart, E x B motion with such velocity shear is not sustainable. With the SCW front width in the ionosphere of the order of 100 km and the speed $v_{scw} \geq 0.1$ MLT hour/min, the time for setting up a steady state at the front should be less than 30 s. As typical Alfvén wave bounce periods are greater than 10^2s, the steady state cannot be reached in the moving front. This is consistent with the observed irregular structure and intermittent development of the SCW front (e.g., Kepko et al., 2015), as well as with more irregular SAPSWS near the substorm onsets.

By the same token, the SAPS-associated ripples on the duskside plasmapause and the giant undulations with wavelengths of a few hundred kilometers are observed shortly after substorm expansions (Goldstein et al., 2005b; Henderson et al., 2010, 2018; Horvath & Lovell, 2016). Their tentative explanation has been given in terms of the shear-flow ballooning (a Kelvin-Helmholtz) instability driven by an intense latitudinal velocity shear in the SAPS region (Henderson et al., 2010, 2018). Another possible interchange instability, the flute (Rayleigh-Taylor) instability, cannot develop because the pressure gradient (∇P_{RC}) near the ring current's inner edge is parallel to the centrifugal force acting on a particle in curved magnetic field lines, which is opposite to the RT condition.

Mishin and Burke (2005) suggested that the Region 2 downward current ($j_z^\downarrow$) can make the system unstable via the so-called current convective instability (Kadomtsev, 1965; Ossakow & Chaturvedi, 1979). For that, the Doppler-shifted frequency of unstable waves should be negative, that is, $\omega' = \omega - k_z u_z < 0$, where $u_z = j_z^\downarrow / n_e e$. Their growth rate in Region 2 is of the order of $\gamma \sim \tan\left(\frac{\alpha}{2}\right) j_p^\downarrow / (\Sigma_P B_I)$ (Volkov & Maltsev, 1986; Xing & Wolf, 2007). Here α is the angle between ∇P_{RC} and the curvature, Σ_P and B_I are the Pedersen conductivity and magnetic field in the conjugate ionosphere (subscript I), respectively. Substituting $j_z^\downarrow = \nabla_\perp(\Sigma_P \mathbf{E}_I)$ in the quasistatic approximation gives $\gamma \sim \tan\left(\frac{\alpha}{2}\right) \nabla \mathbf{v}_d \sim 0.2$ min^{-1}, where $\mathbf{v}_d$ is the SAPS velocity. Unstable perturbations have wavelengths satisfying the condition $10 \ll \lambda_I \ll 1000$ km. In addition, the westward motion of the SCW front should add the term $-k_\perp v_{scw}$ to ω', thus making more favorable generation of shorter scales at higher front speeds.

The ionospheric feedback instability (IFI) (e.g., Lysak, 1991; Trakhtengerts & Feldstein, 1991) in the SAPS region was also considered (Streltsov & Mishin, 2003; Streltsov & Foster, 2004; Streltsov & Mishin, 2018). Free energy for the IFI development comes from the shear convection flow that causes overreflection of Alfvén waves from the ionosphere. Earlier simulations of the subauroral IFI perfectly match weak electromagnetic oscillations at ~0.1 Hz observed on the top of SAPS in the ionosphere (Fig. 5 in Streltsov & Mishin, 2003). Here we consider the connection between the large-scale, quasi-stationary electric field and small-scale ULF electric fields observed by RBSP-A at the beginning of the 17 March 2015 storm (Fig. 8.5). Once created in the equatorial magnetosphere, the electric field penetrates along the ambient magnetic field into the ionosphere and drives the IFI, which generates and amplifies ULF waves traveling back and forth between the hemispheres.

To simulate the RBSP-A 17 March 2015 event, Streltsov and Mishin (2018) utilized a two-fluid, 2-D MHD model in an axisymmetric dipole magnetic field (e.g., Streltsov et al., 2012). The magnetospheric part describes dispersive Alfvén waves in the magnetosphere using equations for the electron parallel momentum and continuity of the density and current. The conducting bottom of the ionosphere is considered as a narrow slab with the uniform density and electric field, as its altitude extent is much less than the parallel wavelength. Therefore, the ionospheric part of the model is given by two equations connecting the perpendicular electric field, $\mathbf{E}_\perp$, and the plasma density in the ionosphere, n_E, with the field-aligned current density, j_z. The resulting system of equations reads

$$\frac{\partial u}{\partial t} + (\mathbf{u}\nabla)u + \frac{e}{m_e}E_z + \frac{1}{m_e n_0}\nabla_z(n_e T_e) + \nu_e u = 0, \quad (8.9)$$

$$\frac{\partial n}{\partial t} + \nabla_\perp(n_e\mathbf{u}) = 0, \quad (8.10)$$

$$\nabla_\perp\left(\mathbf{j}_z + \frac{1}{\mu_0}\left(\frac{1}{c^2} + \frac{1}{v_A^2}\right)\frac{\partial \mathbf{E}_\perp}{\partial t}\right) = 0, \quad (8.11)$$

$$\nabla_\perp(\Sigma_P \mathbf{E}_\perp) \pm j_z = 0, \quad (8.12)$$

and

$$\frac{\partial n_E}{\partial t} - \frac{j_z}{eh} - \alpha n_E^2 + \alpha n_{E0}^2 = 0. \quad (8.13)$$

Here the subscripts z and $\perp$ denote vector components parallel and perpendicular to $\mathbf{B}_0$; $\mathbf{u}$ is the parallel component of the electron velocity; c is the speed of light; $v_A = B_0/\sqrt{\mu_0 n_0 m_i}$ is the Alfvén speed; ν_e is the electron collision frequency; $\Sigma_P = eM_P n_E h/\cos\psi$; $M_P = 10^4$ m^2/sV is the ion Pedersen mobility; e is the electron charge; the sign "+/−" corresponds to the Northern/Southern Hemispheres; and ψ is the angle between the normal to the ionosphere and the dipole magnetic field line at 100 km altitude at $L = 4.9$. The term αn_E^2 represents losses due to recombination with the coefficient $\alpha = 3 \cdot 10^{-7}$ cm^3/s, and the term αn_{0E}^2 represents the unperturbed source of the ionospheric plasma providing the equilibrium state of the ionosphere, n_{0E}.

It should be noted that the ionospheric part of the model can be made more sophisticated. As an example, the dependence of the ion-neutral collision frequency, ν_{in}, on altitude in the ionospheric E region can be included. However, the basic physics of the ionospheric feedback process will remain. For example, the effect of the altitude-profile of ion-neutral collisions in the E region resulting in vertical shear flow was investigated in a series of papers summarized by Trakhtengerts and Feldstein (1991). In particular, the instability threshold for the wave frequency ($f_w \sim$ 0.1-1 Hz) and wavelength ($\lambda_\perp \geq 1$ km) is found after averaging the boundary condition (equation (2) in Trakhtengerts & Feldstein, 1991) over the E layer with the exponential dependence of the ion-neutral collision frequency on altitude. The threshold for low values of $n_{0E} \leq 10^4$ cm^{-3} can be expressed as follows:

$$E_{th} \approx E_0 \cdot \Omega_{ci}/\nu_{i0} \quad \text{mV/m}], \quad (8.14)$$

where Ω_{ci} is the ion gyrofrequency, ν_{i0} ($\gg\Omega_{ci}$) is the ion-neutral collision frequency at the bottom of the E layer, and $E_0 \approx 50$ is a numerical coefficient. As the driving electric field in the simulated event is well beyond the threshold, the use of a simplified slab model is warranted by the substantially reduced computing time.

The background electric field with the maximum amplitude of 49 mV/m in both hemispheres was obtained by electrostatic mapping the low-frequency part, E_0, of the field measured in the equatorial magnetosphere by RBSP-A (Fig. 8.14a) into the ionosphere. The background plasma density in the domain is constructed using data from the 17 March 2015 event and the information about the background electric field. In a general case, the ionospheric plasma densities in the Southern and Northern Hemispheres are not equal to each other. Then, the density in each hemisphere is given by

$$n_0(L,\mu) = \begin{cases} n_{1_{N,S}}(L)(r - r_2) + n_{2_{N,S}}(L), & r_1 < r < r_2 \\ n_{3_{N,S}}(L)e^{-(r-r_2)/r_0} + n_{4_{N,S}}(L)/r, & r > r_2 \end{cases}. \quad (8.15)$$

Here, $r = r(L, \mu)$ is the geocentric distance to the point with the dipole coordinates L and μ; $r_0 = 0.0175$; $r_1 = 1 + 110/R_E$ (near the E-region maximum); $r_2 = 1 + 270/R_E$ (near the F-region peak); and the functions $n_{1_{N,S}}(L)$, $n_{2_{N,S}}(L)$, $n_{3_{N,S}}(L)$, and $n_{4_{N,S}}(L)$ define the density in the ionospheric E region, F region, and in the equatorial magnetosphere. In particular, $n_{4_N}(L) \equiv n_{4_S}(L)$ is chosen to fit the equatorial density profile in Figure 8.5. Functions $n_{2_S}(L)/n_{2_N}(L)$ and $n_{1_S}(L)$ and $n_{1_N}(L)$ are chosen to provide the input values in the southern and northern F and E regions, respectively.

Figure 8.14 synopsizes the simulation results showing the observed (left column) and simulated (right column) electric fields adapted from Streltsov and Mishin (2018). This particular run was conducted for the minimum value of the E-region density in the Northern and Southern Hemispheres of $n_{EN} = 5 \cdot 10^4$ cm^{-3} (corresponds to

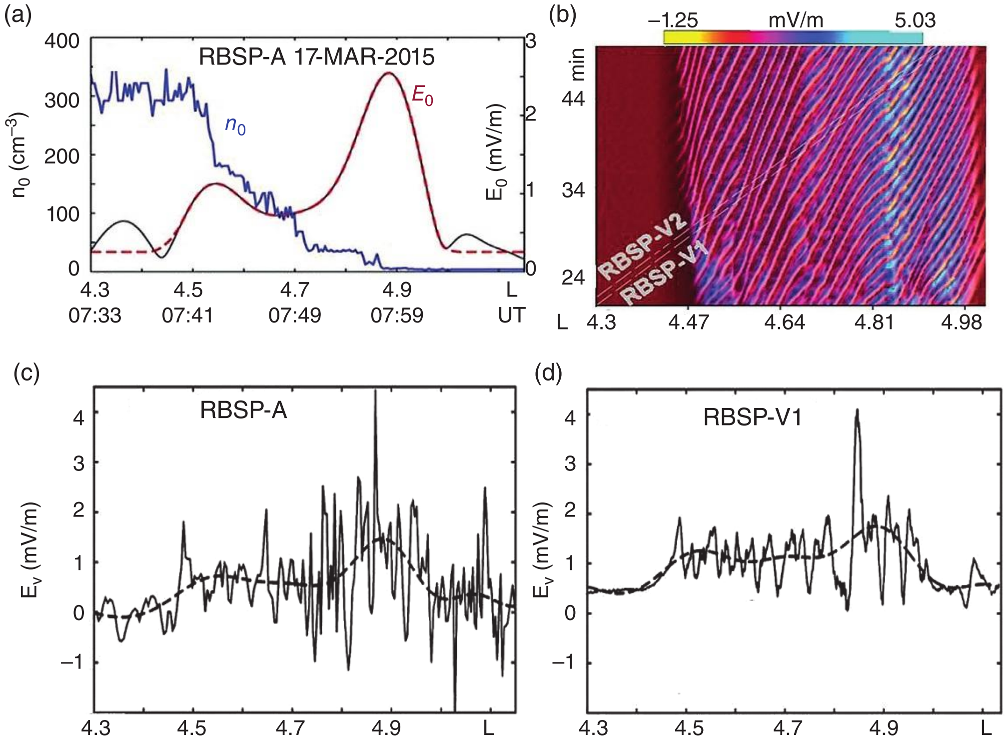

Figure 8.14 (a) The low-frequency electric field amplitude (the red line) and the plasmaspheric density (blue) from RBSP-A. (b) The variation of the simulated electric field in time and space. Two dashed lines show the space-time "trajectories" of the virtual RBSP-V1 and RBSP-V2 satellites in the computational domain. (c) Measured and (d) simulated radial (*V*) component of the electric field with the low-frequency part superimposed (dashed) (see text) (after Streltsov & Mishin, 2018).

Σ_P = 1.6 mho) and $n_{ES} = 10^4$ cm^{-3} (Σ_P = 0.32 mho), respectively. The F-peak density in the Northern and Southern Hemispheres is $n_{FN} = 10^6$ cm^{-3} and $n_{FS} = 2 \cdot 10^5$ cm^{-3}, respectively. The simulated field was obtained "on board" the virtual satellite RBSP-V1 moving along the track of RBSP-A with the same speed. Quite similar results were obtained on RBSP-V2. It is seen that the simulated amplitudes and location of the spatial structures match observations quite well.

These results indicate that the ionospheric feedback interactions contribute significantly to the magnetosphere-ionosphere coupling carried by ULF waves and field-aligned currents. On the other hand, the IFI modeling could not explain the entire features of the strong SAPSWS event near the substorm onset (Mishin et al., 2003), similar to those in Figure 8.9 and Figure 8.11. Future simulations should take the SCW front's irregular structure and intermittent development into account.

8.4.3. Decameter-Scale Irregularities

The gradient-drift and temperature gradient instabilities are considered as feasible driving mechanisms of decameter-scale irregularities (Keskinen et al., 2004; Eltrass & Scales., 2014). These are interchange instabilities driven by polarization fields created by plasma drift in response to initial density perturbations (e.g., Kadomtsev, 1965). For the GDI to develop, the plasma drift velocity, $\mathbf{v}_d = c(\mathbf{E}_0 \times \mathbf{B}_0)/B_0^2$, must be parallel to $\nabla_\perp n$. In this case, the Pedersen current, $\sigma_P \mathbf{E}_0$, creates the polarization electric field, $\mathbf{E}_{pol}$, such that $\mathbf{E}_{pol} \times \mathbf{B}$ drift moves lower (higher) density plasma into regions of higher (lower) density to further enhance initial density perturbations, δn. In the simplest case of short-scale, $k_\perp L_n \gg 1$, "flute" -mode field-aligned irregularities with $k_z = 0$, the GDI growth rate is

$$\gamma_0 \approx \begin{cases} v_d/L_n & \text{at } 4v_d/\nu_{in} \ll L_n = n/|\nabla_\perp n| \\ \sqrt{\nu_{in} v_d/L_n} & \text{at } 4v_d/L_n \gg \nu_{in} \end{cases}. \tag{8.16}$$

Usually, density troughs are longitudinally extended, $|\partial n/\partial x| \gg |\partial n/\partial y| \to 0$; the axes **x** and **y** are directed northward and eastward, respectively. Thus, the GDI development on the trough's poleward wall requires the presence of the eastward electric component. On the other hand, in the presence of field-aligned currents, the eastward field can also drive the instability near the equatorward wall via the current convective instability of oblique oscillations at $2\pi\gamma_0 < k_z j_z / e n_e$.

In general, the meridional temperature and density gradients are antiparallel in the SAPS/SAID-related trough, which is necessary for the TGI. Diamagnetic drifts due to the opposed temperature and density gradients that lead to polarization fields that move lower density hotter regions into higher density colder plasma and vice versa. In the two-fluid approximation, the TGI growth rate is (e.g., Keskinen et al., 2004)

$$\gamma_1 \sim k_\perp c_s r_{ci} (L_n L_T)^{-1/2} - \tau_D^{-1} - \tau_T^{-1}, \qquad (8.17)$$

where $L_T = T/|\nabla_\perp T|$; τ_D^{-1} and τ_T^{-1} are the rates of plasma diffusion and thermal conduction, respectively; and r_{ci} is the ion gyroradius.

Fluid models are limited by irregularities with wavelengths much greater than the ion gyroradius, which is of the order of a few meters in the quiet-time F-region ionosphere (~10 m in the heated SAPS/SAID region). Two-fluid numerical simulations of the GDI development (e.g., Keskinen & Huba, 1990; Guzdar et al.,1998) yield a steady-state power law spectrum of density irregularities, $(\delta n_k / n_0)^2 \propto k^{-p_0}$ due to the wave cascading process. The spectral index in the range of 1 to 10 km is about $p_0 = 2$, which is close to that in Figure 8.11. The TGI growth rate in the kinetic regime appropriate for decameter-scale irregularities is shown in Eltrass et al., (2014, Fig. 2) and Eltrass and Scales (2014, Fig. 2) for various L_n and L_T = 800 and 1,400 km in the quiet-time F-region ionosphere. It increases with $k_\perp$ ($\ll 1/r_{ci}$) and, in the decameter scale, reaches a broad maximum of $\sim 6 \cdot 10^{-4}\Omega_{ci}$ and $\sim 10^{-4}\Omega_{ci}$ for L_n = 50 and 450 km, respectively. The GDI growth rate for $E_0 \sim 1$ mV/m and the same values of $L_{n,\ T}$ is smaller by a factor of 10.

The nonlinear evolution of the TGI, with finite ion gyroradius effects included, was investigated by means of gyrokinetic particle-in-cell simulation techniques with Monte Carlo electron collisions (Eltrass et al., 2014; Eltrass & Scales, 2014). The TGI develops faster and the saturation amplitude increases with electron collision frequency, ν_e. The simulation results show wave cascading from primary kilometer scales into the decameter-scale regime, creating the saturated spectrum of the density fluctuations with the spectral index $p_1 \sim 2$. Therefore, Eltrass and Scales concluded that the observed quiet-time decameter-scale midlatitude irregularities may be produced by the TGI turbulent cascade, such as for the GDI.

As the maximum value of the growth rates increases with $k_{n,\ T} = 1/L_{n,\ T}$ and E_0, the instabilities are supposed to develop much faster in the SAPS and SAID regions. In particular, this implies that the decameter-scale (and smaller scales) waves may be produced directly by the TGI. The presence of the eastward electric field is indicated by the upward vertical velocity. This is largely the case in the SAID and SAPS events, such as shown in Figure 8.2 and Figure 8.11 (the data from F13 near 22:36:00 UT). The downward velocity in the F14 data (Fig. 8.11) indicates the westward electric field. Given $\nabla_x n \cdot \nabla_x T < 0$ on the equatorward wall near 01:06:00 UT, the enhanced irregularities here may be due to the concerted effort of the GDI and TGI. The irregularities in the strong SAPSWS region (Fig. 8.9) can be driven by both instabilities due to strong alternate small-scale field-aligned currents and electric fields (Mishin & Blaunstein, 2008).

8.5. CONCLUSION

We have surveyed multi-spacecraft observations of mesoscale and small-scale wave and plasma structures in the disturbed subauroral ionosphere and plasmasphere and discussed their interrelation and conventional generation mechanisms. In particular, enhanced plasma turbulence is observed in the plasmasphere boundary layer formed by reconnection-injected, mesoscale plasma flows penetrating into the plasmasphere. Three principal sources of free energy for plasma waves are (1) the diamagnetic ion current near the inner boundary of the layer due to the ion pressure gradient, (2) electron diamagnetic currents in the entry layer near the plasma sheet boundary, and (3) anisotropic (ring-like) ion distribution inside, and farther inward of, the inner boundary. Collisionless interactions of plasma waves with plasmaspheric particles lead to plasma heating and acceleration of suprathermal tails, thereby providing downward heat flux and suprathermal electrons that dramatically increase the F-region electron temperature. This results in the formation of specific subauroral density troughs even in the absence of strong electric fields and upward plasma flows. Antiparallel temperature and density gradients inside the subauroral troughs are favorable for the temperature gradient instability. The temperature gradient and the gradient-drift instabilities near the trough walls lead to decameter-scale density irregularities routinely detected by HF radars in the disturbed subauroral ionosphere. Small-scale electromagnetic wave structures (SAPSWS) are observed on the duskside shortly after the substorm onsets. Numerical simulations by means of a two-fluid 2-D MHD model describe the SAPSWS creation in terms of the ionospheric feedback instability, which generates and amplifies ULF waves traveling back and forth between the hemispheres. The instablity is driven by the mesoscale SAPS electric field created in the equatorial magnetosphere and penetrated along the magnetic field into the ionosphere. Although the basic features of mesoscale and small-scale subauroral structures are documented, more careful studies, both experimental and numerical, are needed in order to identify and specify the processes involved in their formation.

ACKNOWLEDGMENTS

EM was supported by the Air Force Office of Scientific Research and AV was supported by the National Research Council Research Associateship Program at the AFRL Space Vehicles Directorate. The Cluster FGM Prime Parameter, EFW, EDI, and the NSF grant AGS 1803702 CIS-CODIF, WBD, and STAFF data sets were obtained through the Cluster Science Data System and the ESA Cluster Active Archive. Van Allen Probes data access was provided through the Johns Hopkins University/Applied Physics Lab Mission Operations Center and the Los Alamos National Laboratory Science Operations Center (www.rbsp-ect.lanl.gov).

REFERENCES

Afonin, V., Bassolo, V., Smilauer, J., & Lemaire, J. (1997). Motion and erosion of the nightside plasmapause region and of the associated subauroral electron temperature enhancement: Cosmos 900 observations. *Journal of Geophysical Research*, *102*, 2093.

Anderson, P., Heelis, R., & Hanson, W. (1991). The ionospheric signatures of rapid subauroral ion drifts. *Journal of Geophysical Research*, *96*, 5785.

Basu, S., et al. (2001). Ionospheric effects of major magnetic storms during the International Space Weather Period of September and October 1999: GPS observations, VHF/UHF scintillations and in situ density structures at middle and equatorial latitudes. *Journal of Geophysical Research*, *106*, 30389.

Basu, S., et al. (2008). Large magnetic storm-induced nighttime ionospheric flows at midlatitudes and their impacts on GPS-based navigation systems. *Journal of Geophysical Research*, *113*, A00A06. doi:10.1029/2008JA013076

Burke, W., Erickson, P., Yang, J., Foster, J., Wygant, J., Reeves, G., & Kletzing, C. (2016). O+ ion conic and plasma sheet dynamics observed by Van Allen Probe satellites during the 1 June 2013 magnetic storm. *Journal of Geophysical Research: Space Physics*, *121*, 4072–4091. doi:10.1002/2015JA021795

Califf, S., Li, X., Wolf, R., Zhao, H., Jaynes, A., Wilder, F., Malaspina, D., et al. (2016). Large-amplitude electric fields in the inner magnetosphere: Van Allen Probes observations of subauroral polarization streams. *Journal of Geophysical Research Space Physics*, *121*, 5294–5306. doi:10.1002/2015JA022252

Carpenter, D. L., & Lemaire, J. (2004). The plasmasphere boundary layer. *Annales de Geophysique*, *22*, 4291–4298. doi:10.5194/angeo-22-4291-2004

Chen, L., Thorne, R., Jordanova, V., & Horne, R. (2010). Clobal simulation of magnetosonic wave instability in the storm time magnetosphere. *Journal of Geophysical Research*, *115*, A11222. doi:10.1029/2010JA015707

Cornwall, J., Coroniti, F. & Thorne, R. (1971). Unified theory of SAR arc formation at the plasmapause. *Journal of Geophysical Research*, *76*, 4428.

Eltrass, A., & Scales, W. (2014). Nonlinear evolution of the temperature gradient instability in the midlatitude ionosphere. *Journal of Geophysical Research: Space Physics*, *119*, 7889–7901. doi:10.1002/2014JA020314

Eltrass, A., Mahmoudian, A., Scales, W., de Larquier, S., Ruohoniemi, J., Baker, J., Greenwald, R. et al. (2014). Investigation of the temperature gradient instability as the source of midlatitude quiet time decameter-scale ionospheric irregularities: Part 2. Linear analysis. *Journal of Geophysical Research: Space Physics*, *119*, 4882–4893. doi:10.1002/2013JA019644

Erickson, P., Foster, J., & Holt, J. (2002). Inferred electric field variability in the polarization jet from Millstone Hill E region coherent scatter observations. *Radio Science*, *37*, 1027. doi:10.1029/2000RS002531

Figueiredo, S., Karlsson, E., &. Marklund, G. (2004). Investigation of subauroral ion drifts and related field-aligned currents and ionospheric Pedersen conductivity distribution. *Annales Geophysicae*, *22*, 923–934.

Foster, J., & Rich, F. (1998). Prompt midlatitude electric field effects during severe magnetic storms. *Journal of Geophysical Research*, *103*, 26,367.

Foster, J., Buonsanto, M., Mendillo, M., Notingham, D., Rich, F., & Denig, W. (1994). Coordinated stable auroral red arc observations: Relationship to plasma convection. *Journal of Geophysical Research*, *99*, 11429–11439.

Foster, J., Erickson, P., Baker, D., Jaynes, A., Mishin, E., Fennel, J., Li, X., et al. (2016). Observations of the impenetrable barrier, the plasmapause, and the VLF bubble during the 17 March 2015 storm. *Journal of Geophysical Research: Space Physics*, *121*, 5537–5548. doi:10.1002/2016JA022509

Foster, J., Erickson, P., Lind, F., & Rideout, B. (2004). Millstone Hill coherent-scatter radar observations of electric field variability in the sub-auroral polarization stream. *Geophysical Research Letters*, *31*, L21803. doi:10.1029/2004GL021271

Foster, J. C., & Vo, H. B. (2002). Average characteristics and activity dependence of the subauroral polarization stream. *Journal of Geophysical Research*, *107*(A12), 1475. doi:10.1029/2002JA009409

Förster, M., Foster, J., Smilauer, J., Kudela, K., & Mikhailov, A. (1999). Simultaneous measurements from the Millstone Hill radar and the Active satellite during the SAID/SAR arc event of the March 1990 CEDAR storm. *Annals of Geophysics*, *17*, 389–404.

Galeev, A., & Sagdeev, R. (1979). Nonlinear plasma theory. In M. Leontovich (Ed.), *Reviews of plasma physics, vol. 7* (pp. 1–156). New York: Consultants Bureau.

Goldstein, J., Burch, J., Sandel, B., Mende, S., C:son Brandt, P., & Hairston, M. (2005b). Coupled response of the inner magnetosphere and ionosphere on 17 April 2002. *Journal of Geophysical Research*, *110*, A03205. doi:10.1029/2004JA010712

Goldstein, J., Kanekal, S., Baker, D., & Sandel, B. (2005a). Dynamic relationship between the outer radiation belt and the plasmapause during March–May 2001. *Geophysical Research Letters*, *32*, L15104. doi:10.1029/2005GL023431

Goldstein, J., Sandel, B., Hairston, M., & Reiff, P. (2003). Control of plasmaspheric dynamics by both convection and subauroral polarization stream. *Geophysical Research Letters*, *30*, 2243–2246. doi:10.1029/2003GL018390

Gorbachev, O., Khazanov, G., Gamayunov, K., & Krivorutsky, K. (1992). A theoretical model for the ring current interaction with the Earth's plasmasphere. *Planetary and Space Science*, *40*, 859–872.

Greenwald, R., Oksavik, K., Erickson, P., Lind, F., Ruohoniemi, J., Baker, J., &. Gjerloev, J. (2006). Identification of the temperature gradient instability as the source of decameter-scale ionospheric irregularities on plasmapause field lines. *Geophysical Research Letters*, *33*, L18105. doi:10.1029/2006GL026581

Gringauz, K. (1983). Plasmasphere and its interaction with the ring current. *Space Science Reviews*, *34*, 245–257.

Gurgiolo, C., Sandel, B., Perez, J., Mitchell, D., Pollock, C., & Larsen, B. (2005). Overlap of the plasmasphere and ring current: Relation to subauroral ionospheric heating. *Journal of Geophysical Research*, *110*, A12217. doi:10.1029/2004JA010986

Guzdar, P., Gondarenko, N., Chaturvedi, P., & Basu, S. (1998). Three-dimensional nonlinear simulations of the gradient drift instability in the high-latitude ionosphere. *Radio Science*, *33*, 1901.

Henderson, M., Donovan, E., Foster, J., Mann, I., Immel, T., Mende, S., & Sigwarth, J. (2010). Start-to-end global imaging of a sunward propagating: SAPS-associated giant undulation event. *Journal of Geophysical Research*, *115*, A04210. doi:10.1029/2009JA014106

Henderson, M., Morley, S., & Kepko, L. (2018). SAPS-associated explosive brightening on the duskside: A new type of onset-like disturbance. *Journal of Geophysical Research: Space Physics*, *123*, 197–210. doi:10.1002/2017JA024472

Horne, R., Wheeler, G., & Alleyne, H. (2000). Proton and electron heating by radially propagating fast magnetosonic waves. *Journal of Geophysical Research*, *105*, 27597–27610.

Horvath, I., & Lovell, B. (2016). Structured subauroral polarization streams and related auroral undulations occurring on the storm day of 21 January 2005. *Journal of Geophysical Research: Space Physics*, *121*. doi:10.1002/2015JA022057

Horwitz, J., Comfort, R., & Chappell, C. (1986). Plasmasphere and plasmapause region characteristics as measured by DE-1. *Advances in Space Research*, *6*, 21–29. doi: 10.1016/0273-1177(86)90313-3

Huba, J., Sazykin, S., & Coster, A. (2017). SAMI3-RCM simulation of the 17 March 2015 geomagnetic storm. *Journal of Geophysical Research Space Physics*, *122*, 1246–1257. doi:10.1002/2016JA023341

Jacobsen, K., & Andalsvik, Y. (2016). Overview of the 2015 St. Patrick's Day storm and its consequences for RTK and PPP positioning in Norway. *Journal of Space Weather and Space Climate*, *6*(A9), 1–12. doi:10.1051/swsc/2016004

Kadomtsev, B. (1965). *Plasma turbulence*. New York: Academic.

Kepko, L., McPherron, R., Amm, O., Apatenkov, S., Baumjohann, W., Birn, J., Lester, M., et al. (2015). Substorm current wedge revisited. *Space Science Reviews*, *190*, 1–46. doi:10.1007/s11214-014-0124-9

Keskinen, M., & Huba, J. (1990). Nonlinear evolution of high-latitude ionospheric interchange instabilities with scale-size-dependent magnetospheric coupling. *Geophysical Research Letters*, *A9*, 15157–15166.

Keskinen, M., Basu, Su., & Basu, Sh. (2004). Midlatitude subauroral small scale structure during a magnetic storm. *Geophysical Research Letters*, *31*, L09811. doi:10.1029/2003GL019368

Khazanov, G. (2011). *Kinetic theory of inner magnetospheric plasma*. New York: Springer.

Khazanov, G., Gamayunov, K., & Jordanova, V. (2003). Self-consistent model of magnetospheric ring current and electromagnetic ion cyclotron waves: The 2–7 May 1998 storm. *Journal of Geophysical Research*, *108*(A12), 1419. doi:10.1029/2003JA009856

Khazanov, G., Gamayunov, K., Gallagher, D., Kozyra, J. & Liemohn, M. (2007). Self-consistent model of magnetospheric ring current and propagating electromagnetic ion cyclotron waves: 2. Wave-induced ring current precipitation and thermal electron heating. *Journal of Geophysical Research*, *112*, A04209. doi:10.1029/2006JA012033

Khazanov, G., Nagy, A., Gambosi, T., Koen, M., & Cariglia, S. (1992). Analytic description of the electron temperature behavior in the upper ionosphere and plasmasphere. *Geophysical Research Letters*, *19*, 1915–1918.

Koustov, A., Drayton, R., Makarevich, R., McWilliams, K., St-Maurice, J.-P., Kikuchi, T., & Frey, H. (2006). Observations of high-velocity SAPS-like flows with the King Salmon SuperDARN radar. *Annals of Geophysics*, *24*, 1591–1608.

LaBelle, J., & Treumann, R. (1988). Current-driven lower hybrid waves at the inner edge of the ring current. *Journal of Geophysical Research*, *93*, 2591–2598.

Ledvina, B. M., Makela, J. J., & Kintner, P. M. (2002). First observations of intense GPS L1 amplitude scintillations at midlatitude. *Geophysical Research Letters*, *29*(14), 1659. doi:10.1029/2002GL014770

Li, X., Baker, D., O'Brien, T., Xie, L., & Zong, Q. (2006). Correlation between the inner edge of outer radiation belt electrons and the innermost plasmapause location. *Geophysical Research Letters*, *33*, L14107. doi:10.1029/2006GL026294

Lysak, R. (1991). Feedback instability of the ionospheric resonant cavity. *Journal of Geophysical Research*, *96*, 1553.

Makarevich, R., & Bristow, W. (2014). Fine structure of subauroral electric field and electron content. *Journal of Geophysical Research Space Physics*, *119*, 3789–3802. doi:10.1002/2014JA019821

Makarevich, R., Kellerman, A., Devlin, J., Ye, H., Lyons, L., & Nishimura, Y. (2011). SAPS intensification during substorm recovery: A multi-instrument case study. *Journal of Geophysical Research*, *116*, A11311.

Mikhailovskii, A. (1974). *Theory of plasma instabilities: Vol. 1. Instabilities of a homogeneous plasma*. New York: Consultants Bureau.

Mishin, E. (2013). Interaction of substorm injections with the subauroral geospace: 1. Multispacecraft observations of SAID. *Journal of Geophysical Research Space Physics*, *118*, 5782–5796. doi:10.1002/jgra.50548

Mishin, E., & Blaunstein, N. (2008). Irregularities within subauroral polarization stream-related troughs and GPS radio interference at midlatitudes. In T. Fuller-Rowell et al. (Eds.), *Mid-latitude ionospheric dynamics and disturbances* (pp. 291–295). Geophysical Monograph Series, vol. *181*. Washington, DC: American Geophysical Union. doi:10.1029/181GM26

Mishin, E., & Burke, W. (2005). Stormtime coupling of the ring current, plasmasphere and topside ionosphere: Electromagnetic and plasma disturbances. *Journal of Geophysical Research*, *110*, A07209. doi:10.1029/2005JA011021

Mishin, E., & Puhl-Quinn, P. (2007). SAID: Plasmaspheric short circuit of substorm injections. *Geophysical Research Letters*, *34*, L24101. doi:10.1029/2007GL031925

Mishin, E., & Sotnikov, V. (2017). The turbulent plasmasphere boundary layer and the outer radiation belt boundary. *Plasma Physics* and *Controlled Fusion*, *59*, 124003. doi:10.1088/1361-6587/aa8481

Mishin, E., Burke, W., & Viggiano, A. (2004). Stormtime subauroral density troughs: Ion-molecule kinetic effects. *Journal of Geophysical Research*, *109*, A10301. doi:10.1029/2004JA010438

Mishin, E., Burke, W., Huang, C., & Rich, F. (2003). Electromagnetic wave structures within subauroral polarization streams. *Journal of Geophysical Research*, *108*, 1309. doi:10.1029/2002JA009793

Mishin, E., Carlson, H., & Hagfors, T. (2000). On the electron distribution function in the F region and airglow enhancements during HF modification experiments. *Geophysical Research Letters*, *27*, 2857–2860.

Mishin, E., Foster, J., Potekhin, A., Rich, F., Schlegel, K., Yumoto, K., Taran, V., et al. (2002). Global ULF disturbances during a stormtime substorm on 25 September 1998. *Journal of Geophysical Research*, *107* (A12), 1486. doi:10.1029/2002JA009302

Mishin, E., Nishimura, Y., & Foster, J. (2017). SAPS/SAID revisited: A causal relation to the substorm current wedge. *Journal of Geophysical Research Space Physics*, *122*, 8516–8535. doi:10.1002/2017JA024263

Mishin, E., Puhl-Quinn, P. A., & Santolik, O. (2010). SAID: A turbulent plasmaspheric boundary layer. *Geophysical Research Letters*, *37*, L07106. doi:10.1029/2010GL042929

Mithaiwala, M., Rudakov, L., & Ganguli, G. (2010). Stability of an ion-ring distribution in a multi-ion component plasma. *Physics* of *Plasmas*, *17*, 042113. doi:10.1063/1.3372842

Moffett, R., Ennis, A., Bailey, G., Heelis, R., & Brace, L. (1998). Electron temperatures during rapid subauroral ion drift events. *Annals of Geophysics*, *16*, 450.

Musher, S., Rubenchik, A., & Sturman, B. (1978). Collective effects associated with lower hybrid heating of plasma. *Plasma Physics*, *20*, 1131–1150.

Newell, P., & Meng, C.-I. (1987). Low altitude observations of dispersionless substorm plasma injections. *Journal of Geophysical Research*, *92*, 10063.

Newton, G., & Walker, J. (1975). Electron density decrease in SAR arcs resulting from vibrationally excited nitrogen. *Journal of Geophysical Research*, *80*, 1325.

Oksavik, K., Greenwald, R., Ruohoniemi, J., Hairston, M., Paxton, L. Baker, J., Gjerloev, J., et al. (2006). First observations of the temporal/spatial variation of the sub-auroral polarization stream from the SuperDARN Wallops HF radar. *Geophysical Research Letters*, *33*, L12104. doi:10.1029/2006GL026256

Ossakow, S., & Chaturvedi, P. (1979). Current convective instability in the diffuse aurora. *Geophysical Research Letters*, *6*, 332–335.

Parkinson, M., et al. (2005) Interhemispheric asymmetries in the occurrence of magnetically conjugate sub-auroral polarisation streams. *Annals of Geophysics*, *23*, 1371–1390.

Pavlov, A., Abe, T., & Oyama, K.-I. (2000). Comparison of the measured and modeled electron densities and temperatures in the ionosphere and plasmasphere during 20–30 January, 1993. *Annals of Geophysics*, *18*, 1257–1271.

Pfaff, R., Liebrecht, C., Berthelier, J.-J., Malingre, M., Parrot, M., & Lebreton, J.-P. (2008). DEMETER satellite observations of plasma irregularities in the topside ionosphere at low, middle, and subauroral latitudes and their dependence on magnetic storms. In T. Fuller-Rowell, et al. (Eds.), *Mid-latitude ionospheric dynamics and disturbances* (pp. 297–311). Geophysical Monograph Series, vol. *181*.Washington, DC: American Geophysical Union. doi:10.1029/181GM26

Porkolab, M. (1978). Parametric processes in magnetically confined CTR plasmas. *Nuclear Fusion*, *18*, 367.

Pröll s, G. (2006). Subauroral electron temperature enhancement in the nighttime ionosphere. *Annals of Geophysics*, *24*, 1871–1885.

Puhl-Quinn, P., Matsui, H., Mishin, E., Mouikis, C., Kistler, L., Khotyaintsev, Y., Décréau, P., et al. (2007). Cluster and DMSP observations of SAID electric fields. *Journal of Geophysical Research*, *112*, A05219. doi:10.1029/2006JA012065

Rodger, A. (2008). The mid-latitude trough: Revisited. In T. Fuller-Rowell, et al. (Eds.), *Mid-latitude ionospheric dynamics and disturbances* (pp. 25–33). Geophysical Monograph Series, vol. *181*.Washington, DC: American Geophysical Union. doi:10.1029/181GM26

Runov, A., Angelopoulos, V., Ganushkina, N., Nakamura, R., McFadden, J., Larson, D., Dandouras, I., et al. (2008). Multipoint observations of the inner boundary of the plasma sheet during geomagnetic disturbances. *Geophysical Research Letters*, *35*, L17S23. doi:10.1029/2008GL033982

Schunk, R., Banks, P., & Raitt, W. (1976). Effect of electric fields and other processes upon the nighttime high-latitude F layer. *Journal of Geophysical Research*, *81*, 3271.

Shapiro, V., Shevchenko, V., Sharma, A., Papadopoulos, K., Sagdeev, R., & Lebedev, V. (1993). Lower-hybrid turbulence at cometary bow wave and acceleration of cometary protons. *Journal of Geophysical Research*, *98*, 1325–1334.

Sotnikov, V., Shapiro, V., & Shevchenko, V. (1978). Macroscopic effects of collapse at lower hybrid resonanse. *Soviet Journal of Plasma Physics*, *4*, 250–258.

St.-Maurice, J.-P., & Torr, D. (1978). Nonthermal rate coefficients in the ionosphere: The reactions of O^+ with N_2, O_2, and *NO*. *Journal of Geophysical Research*, *83*, 969.

Streltsov, A., & Foster, J. (2004). Electrodynamics of the magnetosphere-ionosphere coupling in the nightside subauroral zone. *Physics of Plasmas*, *11*, 1260–1267. doi:10.1063/11647139

Streltsov, A., & Mishin, E. (2003). Numerical modeling of localized electromagnetic waves in the nightside subauroral zone. *Journal of Geophysical Research*, *108*, 1332. doi:10.1029/2003JA009858

Streltsov, A., & Mishin, E. (2018). Ultra-low-frequency electrodynamics of magnetosphere-ionosphere interactions near the plasmapause during substorms. *Journal of Geophysical Research: Space Physics*, *123*, 7441–7451. https://doi.org/10.1029/2018JA025899

Streltsov, A., Jia, N., Pedersen, T., Frey, H., & Donovan, E. (2012). ULF waves and discrete aurora. *Journal of Geophysical Research*, *117*, A09227. doi:10.1029/2012JA017644

Trakhtengertz, V., & Feldstein, A. (1991). Turbulent Alfvén boundary layer in the polar ionosphere: 1. Excitation conditions and energetics. *Journal of Geophysical Research*, *96*, 19363–19374.

Viggiano, A., & Williams, S. (2001). Ion-molecule kinetics at high temperatures (300–1800 K): Derivation of internal energy dependencies. *Advances in Gas-Phase Ion Chemistry*, *4*, 85–136.

Volkov, M., & Maltsev, Y. (1986). A slot instability of the inner boundary of the plasma layer. *Geomagnetism and Aeronomy*, *English Trans.*, *26*, 671–678.

Xing, X., & Wolf, R. (2007). Criterion for interchange instability in a plasma connected to a conducting ionosphere. *Journal of Geophysical Research*, *112*, A12209. doi:10.1029/2007JA012535

Yizengaw, E., & Moldwin, M. (2005). The altitude extension of the mid-latitude trough and its correlation with plasmapause position. *Geophysical Research Letters*, *32*, L09105. doi:10.1029/2005GL022854

APPENDIX

As an example, we estimate the turbulent heating rate in the entry layer for the 18 March 2002 SAID event (Mishin, 2013). For azimuthal electron drift currents $j_d \sim$ 10–20 nA/m^2 and the hot electron density $N_e \leq 1$ cm^{-3}(Fig. 8.3), the drift speed, $u_d = 6\cdot\frac{j_d\,[\mathrm{nA/m^2}]}{N_e\,[\mathrm{cm^{-3}}]}$, is greater than 60–120 km/s. Such a current can drive various plasma modes in magnetized cold plasma including LH and MS waves (e.g., Mikhailovskii, 1974). As the drift speed, u_d, exceeds the thermal speed of plasmaspheric H^+ ions, $v_{pi} \approx$ 15–30 km/s at the temperature T_{pi} = 1–4 eV, the instability develops in the so-called modified two-stream regime (e.g., Galeev & Sagdeev, 1979). As a result, at $\omega_{pe} \gg \omega_{ce}$ LH waves of $\omega_{lh} = \omega_{\mathbf{k}} = \omega_{lhr}\sqrt{1 + k^2 r_*^2 + \eta_k^2} \approx k_\perp u_d$, with $k_\perp u_d/k_z \gg v_{pe}$ and $k_\perp \sim 0.3/r_*$, grow at a rate $\gamma_{lh} = a_{lh}\omega_{lhr} \gg \omega_{ci}$ ($\alpha_{lh} \geq 0.1$). Here ω_{pe} (ω_{ce}) is the electron plasma (cyclotron) frequency, r_{ce} (v_{pe}) is the thermal electron gyroradius (thermal speed); $r_* = r_{ce}\sqrt{3/4 + 3T_{pi}/T_{pe}}$; $k_z/k_\perp$ is the parallel/perpendicular component of the wavevector k; and $\eta_k = \sqrt{m_i/m_e}k_z/k$. Similarly, short-wavelength MS waves of $\omega_{\mathbf{k}} \approx k_\perp u_d \gg \omega_{ci}$ and $|\omega_{\mathbf{k}} - s\omega_{ci}| \gg k_z v_{pe}$ are excited at a rate $\gamma_{ms} = \alpha_{ms}\omega_{ci}$ ($\alpha_{ms} > 1$).

The power of broadband LH waves at $\omega_{lh} > \sqrt{2}\omega_{lhr}$ is defined by induced scattering (also known as nonlinear Landau damping) by thermal electrons and ions, $\omega_{\mathbf{q}} \approx \omega_{\mathbf{k}} - |k_z - q_z|v_{pe}$ and $\omega_{\mathbf{q}} \approx \omega_{\mathbf{k}} - |\mathbf{k} - \mathbf{q}|v_{pi}$, respectively (e.g., Galeev & Sagdeev, 1979). Porkolab (1978) and Musher et al. (1978) described in detail nonlinear interactions of unstable LH waves. Well above the collisional threshold, $\gamma_{ind} \gg \nu_e$, induced scattering by electrons, with the rate $\gamma_{ind}^{(e)} \approx \omega_{lhr}\frac{m_e}{m_i}\frac{\omega_{pe}^2}{\omega_{ce}^2} W_{lh}/n_p T_{pe}$ is the chief contributor at $\omega_{\mathbf{k}} \leq 3\omega_{lhr}$; the scattering on ions proceeds with $\gamma_{ind}^{(i)} \approx \frac{\omega_{lhr}}{\omega_{lh}}\gamma_{ind}^{(e)}$. Here $W_{lh} \approx \left(\frac{\omega_{pe}}{\omega_{ce}}\right)^2 \left|\delta E_{lh}^2\right|/8\pi$ is the energy density of LH waves with the rms amplitude δE_{lh}, and ν_e is the frequency of electron elastic collisions.

At saturation, the excitation rate, γ_{lh}, is balanced by $\gamma_{ind}^{(e)}$ to yield the energy density of the excited (primary) waves, $W_{lh}^{(0)} \approx \left(\gamma_{lh}\omega_{lhr}/\omega_{pe}^2\right) n_p T_{pe}$. For $\omega_{ce}^2/\omega_{pe}^2 \sim 0.1$ in the entry layer, one gets $W_{lh}^{(0)} \sim 5\cdot 10^{-6} n_p T_{pe}$ and $\delta E_{lh}^{(0)} \sim 0.3$ mV/m at the plasma density $n_p \sim 10$ cm^{-3} and $T_{pe} \sim 1$ eV. The primary LH waves serve as a pump for exciting secondary waves that, in turn, serve as a pump for tertiary waves, etc. As the frequency change at each step "s" is small, $\delta\omega_q^{(s)}/\omega_q^{(s)} \sim qr_* \ll 1$, and hence $\gamma_{ind}^{(s)} \sim \gamma_{ind}^{(s+1)}$, the ultimate "cascading" spectrum consists of $S_* \sim (qr_*)^{-1}$ overlapping spectral peaks of the amplitude $\sim \delta E_{lh}^{(0)}$. This usual weak-turbulence spectrum (e.g., Galeev & Sagdeev, 1979) is consistent with the wave color spectrograms around ω_{lhr} (Fig. 8.2). As at each step, the core electron/ion distribution is heated with the rate $Q_{e/i} \approx S_*^{-1/2}\gamma_{ind}^{(e/i)} W_{lh}$ (e.g., Musher et al., 1978), the temperature increases as $n_p dT_{pe/i}/dt \sim S_* Q_{e/i}$. For the parameters in the entry layer, the characteristic heating rate, $\tau_T^{-1} \sim S_*^{1/2}\left(\gamma_{lh}^2\omega_{lhr}/\omega_{pe}^2\right)$, yields the heating time, τ_T, less than ~ 10 min.

At $\gamma_{lh}/\nu_e \gg 1$, a significant part of the *lh* energy is accumulated in the low-frequency spectral region $\omega_{lh} < \sqrt{2}\omega_{lhr}$, where wave coupling is dominated by the lower hybrid collapse with the threshold $W_{lh}^*/n_p T_{pe} \approx \left(qr_*\sqrt{\frac{m_e}{m_i}}\frac{\omega_{ce}}{\omega_{pe}}\right)^2 \sim 10^{-7}$ (Musher et al., 1978; Sotnikov et al., 1978; Shapiro et al., 1993). In the course of collapse, the field-aligned, l_z, and transverse, $l_\perp$, dimensions of cavities decrease, thereby shifting the trapped *lh*-spectrum to smaller phase velocities ($u_\lambda \sim \omega_{lr}\lambda_p \to u_{\min}$ and $v_{\perp\lambda} \sim \omega_{lr}\lambda_\perp$). Ultimately, the LH-wave energy in collapsing cavities is absorbed by cold-plasma particles via Landau or transit-time damping to produce suprathermal tail distributions of field-aligned electrons (at $10T_{pe} < \varepsilon_\parallel < \varepsilon_{\max} \sim 10^2 T_{pe}$) and mainly transverse ions (at $\varepsilon_\perp > 10T_i$).